The Meteoritical Society

Meteoritics & Planetary Science 1–21 (2024)
doi: 10.1111/maps.14269

A reappraisal of the petrogenesis of Apollo 17 lunar dunites 72415-72417: Relics of the deep lunar mantle?

K. K. BHANOT[1,2], H. DOWNES[1,2,3]*, B. G. RIDER-STOKES[4], E. S. JENNINGS[1,3], M. ANAND[2,4], J. F. SNAPE[5,6], and M. J. WHITEHOUSE[5]

[1]School of Natural Sciences, Birkbeck University of London, London, UK
[2]Natural History Museum, London, UK
[3]UCL/Birkbeck Centre for Planetary Sciences, University College London, London, UK
[4]School of Physical Sciences, The Open University, Milton Keynes, UK
[5]Department of Geosciences, Swedish Museum of Natural History, Stockholm, Sweden
[6]Department of Earth and Environmental Sciences, University of Manchester, Manchester, UK

***Correspondence**
H. Downes, School of Natural Sciences, Birkbeck University of London, Malet Street, London WC1E 7HX, UK.
Email: h.downes@bbk.ac.uk

(Received 16 July 2023; revision accepted 17 September 2024)

Abstract–Lunar dunite samples 72415–72417, collected by Apollo 17 astronauts from a South Massif boulder in the Taurus–Littrow valley, are crushed breccias composed of several types of olivine- and clinopyroxene-rich clasts, some of which are (or contain) intergrowths of Cr-spinel and pyroxenes or plagioclase. Among the clasts are ellipsoidal symplectites of Cr-spinel and pyroxene, up to 300 μm in diameter, which have bulk compositions consistent with those of olivine + garnet. These symplectites are inferred to originally have been olivine + Mg-Cr-rich garnet (pyrope–uvarovite) that formed deep in the lunar mantle and were subsequently transported closer to the lunar surface (spinel- or plagioclase-peridotite stability fields), perhaps during gravitationally driven overturn. Abundant microsymplectite (30 μm diameter) intergrowths of Cr-spinel and pyroxene inside olivine grains, many associated with inclusions of plagioclase and augite, formed during a later decompression event (perhaps excavation to the lunar surface). These inclusions have not previously been recorded in these samples and could be responsible for earlier reports of igneous zoning in olivine. Electron backscatter diffraction data show evidence of high shock pressures (>50 GPa), which are inferred to have occurred during the impact which excavated the dunites from the shallow anorthite-bearing lunar mantle. Apatite veinlets post-date the shock metamorphism and have been dated to 3983 ± 72 Ma and 3913 ± 118 Ma by the U–Pb method. This age is consistent with that inferred for the Imbrium impact basin, suggesting that the dunite was finally excavated from the mantle during formation of the Imbrium basin.

INTRODUCTION

Dunite samples 72415–72417 were chipped from a large clast in Boulder 3 at Station 2 in the Taurus–Littrow Valley. Astronaut H. Schmitt recognized the rock as being composed of "light pastel green material in a paler matrix" and suggested that it was "olivine and something." The samples are classified as cataclastic dunites and are generally composed of 93% olivine, 4% plagioclase, and 3% pyroxene (Dymek et al., 1975). The dunites also contain small masses of symplectites (intergrowths of Cr-spinel and other minerals) and minor apatite.

The 72415-7 dunites attracted significant attention and study in the immediate post-Apollo era (e.g., Albee

et al., 1975; Bell et al., 1975; Bell & Mao, 1975; Dymek et al., 1975; Laul & Schmitt, 1975), but their formation remained uncertain. Interpretations fall into two main categories: (1) they belong to the Mg-suite of lunar intrusive rocks and crystallized in the lunar crust (i.e., they are magmatic cumulates), and (2) they are (or were) samples of the lunar mantle analogous to mantle dunite xenoliths on Earth (i.e., they are tectonized peridotites). Ryder (1992) reported that olivine crystals in 72415 showed chemical zoning, and thus, he inferred that the dunites had formed at a shallow level in the lunar crust. Furthermore, he did not recognize any shock-induced textures, and so considered that the rock had not experienced a deep excavating impact, so that a mantle origin was unlikely. Following Ryder (1992), Warren (1993) and Shearer, Elardo, et al. (2015) also inferred that the dunites belong to the shallow crustal Mg-suite. In contrast, Schmitt (2016) suggested that the Cr-spinel symplectites in the dunites show evidence of having been formed at great depth in the lunar mantle, and that these samples had been brought nearer to the lunar surface by mantle overturn, prior to final impact excavation.

To address the debate about the petrogenesis of 72415-7, we have undertaken a re-examination of these samples using modern methods. Petrography and mineral chemistry were evaluated using scanning electron microscopy (SEM), electron microprobe analyses (EMPA), and computed X-ray tomography (CT) scanning. Electron backscatter diffraction (EBSD) was used to evaluate microstructural modifications of olivine and apatite, and U–Pb isotopic dating method by secondary ion mass spectrometry (SIMS) was used to determine the age of the apatites.

MATERIALS AND METHODS

Samples for this study were provided by the NASA Apollo curatorial staff at Johnson Space Center, including thin sections of 72415,53 and 72417,1 (Figure S1), and several small rock fragments of 72415,4 and 72417,9003. Thin section 72415,53 was gridded to provide locations of EMPA results (Figure S2). 72417,1 was composed of 10 fragments, which have been labeled A-J for clarity (Figure S3). Thin section analyses by optical microscope and electron microprobe were performed at the Birkbeck University of London and the Natural History Museum (NHM) in London. Backscatter electron (BSE) images and elemental maps were acquired with the Jeol JXA8100 Superprobe with an Oxford Instruments Aztec energy-dispersive system (EDS) at Birkbeck. Mosaics of individual images BSE and X-ray element maps of the thin sections were collected on a Zeiss EVO15LS scanning electron microscope at the NHM are presented in Figure S1.

Column conditions for EDS analysis included an accelerating voltage of 15 kV, a beam current of 10 nA, and a beam diameter of 1 μm. EDS analyses were calibrated against standards of natural silicates, oxides, and Specpure® metals. An XPP (φ)ρz correction was applied. Mineral analyses were also carried out at the NHM, London, by wavelength-dispersive spectrometry (WDS) using a Cameca SX100 electron probe microanalyzer. WDS data were calibrated against silicates, major element oxides, and pure metals. Column conditions include an accelerating voltage of 20 kV, a current of 20 nA, and a beam diameter of 1 μm. All EMPA data in Table 1 are by WDS, except for those in two of the smallest Cr-spinel symplectites (types C and D, see below for definitions) that could not be properly analyzed by WDS because of their small size. Data collected by EDS are provided for these minerals in Table 1. 72417,1 was analyzed by WDS on the Jeol JXA8100 Superprobe at Birkbeck (Table 2). WDS data were calibrated against silicates, major element oxides, and pure metals. Column conditions include an accelerating voltage of 20 kV, a current of 25 nA, and a beam diameter of 1 μm. BSE images of analyzed sites presented in Table 1 are shown in Figure S7 and can be linked to the locations in the gridded image shown in Figure S2, via the grid references given in Table S1.

Bulk analyses of the largest (type A) symplectites (see below for descriptions of the different types of symplectite in the samples) were initially estimated from EDS area scans, using a free-hand loop tool to outline the area of interest. This method produces only an approximate estimate of the composition of the area, as it depends on both the percentage of the minerals inside the loop and on the XPP (φ)ρz correction. Therefore, an alternative method was used. A bulk analysis of one such symplectite (that shown in Figure 2a) was reconstructed by estimating the mineral modes and calculating a bulk with these modes from the average of WDS measurements of those phases within the symplectite (Table 3). Mineral modes were estimated by applying grayscale thresholds to a BSE image in ImageJ for clinopyroxene, spinel, and orthopyroxene, and excluding fractures where possible. The bulk symplectite composition was then recalculated as a garnet–olivine mixture, to test the hypothesis that type A symplectites result from garnet reaction with olivine. This calculation was performed with the following assumptions: (1) that Mg#garnet = Mg#olivine = Mg#bulk; (2) that all Ca, Cr, Mn, and Al were hosted by various garnet endmembers, with remaining unassigned Mg, Fe, and Si used up in olivine components; (3) that all Fe was present as Fe^{2+}, which is appropriate for lunar conditions. The reconstruction was possible with a small excess (5%) SiO_2 component remaining unassigned.

The 3-D textures of 72415,4 and 72417,9003 were investigated using micro-CT analysis. Both samples comprised three small angular fragments with typical

TABLE 1. Electron microprobe data for minerals in 72415,53.

Site of interest	*n*	SiO_2	1σ	TiO_2	1σ	Al_2O3	1σ	Cr_2O_3	1σ	FeO	1σ	MnO	1σ	MgO	1σ	CaO	1σ	Na_2O	1σ	Total	Mg#	Cr#	Wo	En	Fs	An	Ab
Olivine																											
5 (type A)	3	40.62	*0.66*	-	-	-	-	0.57	*0.34*	11.17	*0.16*	0.13	*0.02*	46.34	*1.35*	0.31	*0.27*	-	-	99.4	88.1	-	-	-	-	-	-
14 (type A)	2	40.94	*0.07*	-	-	-	-	0.12	*0.01*	11.63	*0.06*	0.12	*0.02*	47.52	*0.12*	0.14	*0.01*	-	-	100.4	87.9	-	-	-	-	-	-
G (type A)	3	40.92	*0.03*	-	-	-	-	0.10	*0.02*	11.59	*0.03*	0.12	*0.01*	47.53	*0.05*	0.12	*0.01*	-	-	100.4	88.0	-	-	-	-	-	-
B (type B)	6	40.56	*0.07*	-	-	-	-	0.19	*0.15*	11.69	*0.09*	0.13	*0.01*	47.38	*0.13*	0.13	*0.02*	-	-	100.2	87.8	-	-	-	-	-	-
4 (type B)	3	40.71	*0.06*	-	-	-	-	0.08	*0.01*	11.67	*0.01*	0.13	*0.01*	47.55	*0.08*	0.12	*0.02*	-	-	100.3	87.9	-	-	-	-	-	-
8a (type B)	3	40.84	*0.13*	-	-	-	-	0.05	*0.01*	11.76	*0.01*	0.13	*0.01*	47.36	*0.04*	0.13	*0.02*	-	-	100.3	87.8	-	-	-	-	-	-
20a (type B)	3	40.28	*0.66*	-	-	-	-	0.51	*0.70*	11.68	*0.08*	0.12	*0.02*	47.18	*0.25*	0.13	*0.01*	-	-	99.9	87.8	-	-	-	-	-	-
C (type B)	3	40.97	*0.06*	-	-	-	-	0.18	*0.04*	11.53	*0.04*	0.12	*0.01*	47.58	*0.04*	0.13	*0.02*	-	-	100.5	88.0	-	-	-	-	-	-
3 (EDS) (type D)	3	40.25	*0.61*	-	-	-	-	-	-	11.81	*0.01*	0.13	*0.15*	47.89	*0.50*	-	-	-	-	100.1	87.9	-	-	-	-	-	-
Clinopyroxene																											
5 (type A)	3	54.67	*0.32*	0.29	*0.04*	1.18	*0.10*	0.87	*0.04*	2.69	*0.05*	-	-	18.03	*0.23*	22.56	*0.19*	-	-	100.3	92.3	-	45.3	50.4	4.2	-	-
14 (type A)	1	54.67		0.13	-	1.26	-	0.97	-	2.84	-	0.08	-	18.38	-	22.20	-	-	-	100.5	92.0	-	44.3	51.1	4.6	-	-
G (type A)	1	54.37		0.19	-	1.27	-	0.98	-	2.74	-	0.09	-	18.03	-	22.52	-	-	-	100.2	92.1	-	45.2	50.4	4.4	-	-
8a (type B)	3	53.74	*0.21*	0.72	*0.10*	1.79	*0.15*	0.68	*0.04*	2.67	*0.13*	-	-	17.65	*0.21*	22.84	*0.36*	-	-	100.1	92.2	-	46.1	49.6	4.2	-	-
C (type B)	3	54.16	*0.37*	0.23	*0.02*	1.13	*0.06*	0.91	*0.14*	3.23	*0.31*	-	-	18.99	*0.79*	21.17	*1.11*	-	-	99.8	91.3	-	42.2	52.7	5.0	-	-
3 (EDS) (type D)	4	53.04	*0.12*	0.12	*0.10*	1.19	*0.14*	0.84	*0.15*	3.02	*0.19*	-	-	18.07	*0.07*	23.21	*0.26*	-	-	99.5	91.4	-	45.6	49.3	5.1	-	-
Orthopyroxene																											
14 (type A)	2	55.87	*0.95*	0.12	*0.01*	1.01	*0.15*	1.90	*0.20*	7.33	*0.03*	-	-	33.45	*0.12*	0.99	*0.02*	-	-	100.7	89.1	-	1.8	87.3	10.9	-	-
8a (type B)	3	56.78	*0.84*	0.33	*0.07*	1.07	*0.19*	0.50	*0.04*	6.57	*0.56*	-	-	32.10	*1.74*	3.48	*3.20*	-	-	100.8	89.7	-	6.5	83.7	9.8	-	-
Cr-spinel																											
5 (type A)	2	0.35	*0.34*	0.63	*0.04*	16.19	*0.95*	51.52	*1.22*	17.86	*1.06*	0.20	*0.04*	10.66	*0.86*	0.50	*0.25*	-	-	97.9	51.5	68.1	-	-	-	-	-
14 (type A)	2	0.40	*0.04*	0.61	*0.13*	16.20	*0.49*	50.99	*0.40*	18.88	*0.31*	0.22	*0.01*	10.07	*0.42*	0.47	*0.08*	-	-	97.8	48.7	67.9	-	-	-	-	-
G (type A)	2	0.22	*0.10*	0.64	*0.13*	17.48	*1.03*	50.06	*0.71*	19.41	*0.08*	0.23	*0.01*	10.17	*0.05*	0.27	*0.00*	-	-	98.5	48.3	65.8	-	-	-	-	-
B (type B)	2	0.07	*0.02*	1.52	*0.17*	22.01	*2.97*	44.66	*2.95*	18.30	*0.64*	0.20	*0.01*	11.52	*0.70*	0.12	*0.02*	-	-	98.4	52.9	57.7	-	-	-	-	-
4 (type B)	3	0.19	*0.14*	0.98	*0.26*	26.27	*1.63*	41.17	*1.65*	16.81	*0.87*	0.17	*0.02*	12.67	*0.66*	0.26	*0.13*	-	-	98.5	57.3	51.2	-	-	-	-	-
20a (type B)	2	0.35	*0.30*	0.50	*0.02*	17.27	*2.62*	50.67	*3.60*	19.37	*0.61*	0.21	*0.01*	10.04	*0.74*	0.22	*0.13*	-	-	98.6	48.0	66.3	-	-	-	-	-
C (type B)	3	0.15	*0.05*	0.58	*0.03*	17.81	*0.21*	50.45	*0.30*	18.08	*0.32*	0.20	*0.01*	11.04	*0.10*	0.27	*0.06*	-	-	98.6	52.1	65.5	-	-	-	-	-
3 (EDS) (type D)	3	0.10	*0.04*	0.37	*0.21*	17.06	*0.52*	51.89	*0.39*	18.37	*0.61*	1.15	*0.30*	10.99	*0.28*	0.44	*0.16*	-	-	100.4	51.6	67.1	-	-	-	-	-
6 (EDS) (linear channel)	3	1.16	*0.28*	0.54	*0.09*	12.38	*0.11*	53.43	*1.41*	20.33	*0.43*	1.23	*0.11*	11.19	*0.97*	0.07	*0.05*	-	-	100.3	49.5	74.3	-	-	-	-	-
Plagioclase																											
B (type B)	3	44.24	*0.97*	-	-	34.81	*0.13*	-	-	0.31	*0.04*	-	-	-	-	18.76	*0.26*	0.59	*0.20*	98.7	-	-	-	-	-	94.6	5.4
4 (type B)	3	43.52	*0.07*	-	-	35.99	*0.15*	-	-	0.32	*0.15*	-	-	-	-	19.52	*0.38*	0.25	*0.07*	99.6	-	-	-	-	-	99.4	0.6
8a (type B)	3	45.79	*0.12*	-	-	34.17	*0.32*	-	-	0.25	*0.05*	-	-	-	-	18.27	*0.33*	0.80	*0.07*	99.3	-	-	-	-	-	92.7	7.3
20a (type B)	3	44.91	*1.11*	-	-	33.94	*1.08*	-	-	0.35	*0.03*	-	-	-	-	18.81	*0.13*	0.61	*0.22*	98.6	-	-	-	-	-	94.5	5.5
C (type B)	3	45.05	*1.28*	-	-	34.81	*0.94*	-	-	0.42	*0.03*	-	-	-	-	18.68	*0.71*	0.63	*0.35*	99.6	-	-	-	-	-	94.3	5.7

Note: Average of n measurements. 1σ is standard deviation.

TABLE 2. 72417,1 WDS analysis.

Sample	*n*	Texture	SiO_2	1σ	TiO_2	1σ	Al_2O_3	1σ	Cr_2O_3	1σ	FeO	1σ	MnO	1σ	MgO	1σ	CaO	1σ	Total	Mg#	Cr#	Wo	En	Fs
Olivine																								
Fragment A	4	olt[a]	40.16	*0.40*	-	-	-	-	0.04	*0.01*	11.88	*0.13*	0.14	*0.02*	47.79	*0.10*	0.09	*0.01*	100.10	87.76	-	-	-	-
Fragment B	3	olt	39.89	*0.2*	-	-	-	-	0.03	*0.01*	47.02	*0.05*	0.08	*0.01*	12.58	*0.16*	0.13	*0.01*	99.72	86.95	-	-	-	-
Fragment F	4	olt	39.33	*0.32*	-	-	-	-	0.03	*0.02*	12.86	*0.08*	0.12	*0.01*	47.07	*0.07*	0.13	*0.02*	99.54	86.71	-	-	-	-
Clinopyroxene																								
Fragment B	3	olt	51.57	*0.20*	0.48	*0.08*	1.39	*0.19*	0.76	*0.17*	3.06	*0.05*	0.09	*0.02*	17.83	*0.10*	23.19	*0.30*	98.37	91.20	-	45.96	49.19	4.85
Fragment F	7	olt	52.54	*0.42*	0.44	*0.07*	1.46	*0.21*	0.71	*0.08*	3.03	*0.09*	0.09	*0.02*	18.11	*0.22*	22.99	*0.26*	99.37	91.02	-	45.34	49.77	4.89
Fragment A	5	type C	50.78	*1.13*	0.44	*0.09*	1.54	*0.28*	1.87	*1.54*	3.34	*0.41*	0.09	*0.02*	17.95	*0.33*	22.51	*1.03*	98.52	90.58	-	44.88	49.82	5.30
Orthopyroxene																								
Fragment B	1	olt	54.81	-	0.16	-	0.84	-	0.61	-	7.71	-	0.14	-	33.20	-	1.04	-	98.51	88.47	-	1.95	86.63	11.42
Fragment F	7	olt	55.32	*0.46*	0.25	*0.03*	1.28	*0.15*	0.55	*0.08*	32.78	*0.27*	1.45	*0.42*	7.49	*0.12*	0.14	*0.01*	99.25	88.42	-	0.36	26.96	72.68
Cr-spinel																								
Fragment B	3	olt	0.60	*0.18*	0.39	*0.02*	20.09	*3.76*	47.17	*4.61*	20.62	*0.59*	0.28	*0.06*	10.83	*0.87*	0.02	*0.01*	100.01	33.64	61.16	-	-	-
Fragment F	3	olt	0.89	*0.71*	0.44	*0.07*	28.85	*11.27*	38.54	*12.21*	18.36	*2.46*	0.21	*0.06*	12.42	*2.76*	0.45	*0.39*	100.16	54.68	47.26	-	-	-
Fragment A	1	type C	0.60	-	0.39	-	20.09	-	47.17	-	20.62	-	0.28	-	10.83	-	0.02	-	100.01	48.35	61.16	-	-	-

Note: Average of n measurements. 1σ is standard deviation.
[a]Olivine texture (olt) means regions of olivine grains containing complex structures of cpx, an and cr-spinel.

TABLE 3. Bulk compositions of two Cr–spinel–pyroxene clusters (SPC) in 72415,53, using an EDS area scan inside a free-hand loop (analyzed at Birkbeck). Recalculation of garnet composition (after subtraction of olivine) as detailed in Methodology.

wt%	Bulk, site of interest 8	Garnet, calculated[a]	Olivine, calculated
SiO_2	41.53	37.99	39.41
TiO_2	0.25		
Al_2O_3	4.88	7.65	
Cr_2O_3	13.15	20.63	
FeO	6.89	2.37	17.56
NiO	0.01	0.00	
MnO	0.12	0.18	
MgO	16.90	5.82	43.03
CaO	16.17	25.36	
Total	99.89	100.00	100.00
Mg#	81.4	81.4	81.4
Mode wt%		64.0	30.8
Andradite		0.0	
Uvarovite		64.4	
Knorringite		0.0	
Spessartine		0.4	
Almandine		5.2	
Grossular		7.1	
Pyrope		22.8	

[a]See text for details.

diameters of 1–2 mm. As EMPA analysis had revealed an uneven distribution of Cr-spinel, only the larger fragments were selected for analysis. Micro-CT data were collected on a high-resolution Zeiss Xradia Versa 520 CT scanner at the NHM, London. Because of their small size, the samples were scanned without any preparation other than being placed in plastic bags, packed to restrict movement during analysis, placed inside a plastic tube, and mounted on the sample stage of the instrument. Typical data collection parameters were a source setting of 70 kV and 86 μA, exposure time of 10s, LE1 source filter, optical magnification of 4.0228, and a pixel size resolution of 1.3985 μm. 3-D and 2-D slice images were processed using the Avizo and ORS Dragonfly 3-D visualization software suites.

Thin-sections of 72415,53 and 72417 were investigated using a Zeiss Crossbeam 550 with an Oxford Instruments Symmetry 2 EBSD detector at the Open University, Milton Keynes, United Kingdom. High-resolution EDS smart maps were collected using an Oxford Instruments Ultim Extreme and an Oxford Instruments Ultim Max detector. The sample was tilted to 70° and an electron beam was used to generate EBSD "maps," consisting of electron backscatter diffraction patterns (EBSPs) acquired at 0.1–1 μm step sizes. The

beam conditions used for both EDS and EBSD analyses were an incident beam of 1–2 nA current and a 20 kV accelerating voltage at a working distance of 12 mm. Data were processed offline using Aztec Crystal, where a "wildspike" correction and noise reduction (level 8) were applied. Microstructural data were initially interpreted using band contrast (BC) images. BC describes the intensity of Kikuchi bands in relation to the overall EBSP, highlighting the crystallinity of the analyzed phases. Inverse pole figure (IPF) maps were colored according to the orientation of the studied phase relative to the crystal axes, allowing differentiation of phase orientations. Finally, the degree of internal grain misorientation was visualized using grain reference orientation deviation maps. Grains are defined by misorientation angles >10°, while subgrains are defined by orientations <10°. Olivine diffraction patterns were matched to an orthorhombic symmetry with parameters of $a = 9.5252$, $b = 5.6889$, $c = 4.5968$ and $\alpha = 90°$, $\beta = 90°$, $\gamma = 90°$ (Inorganic Crystal Structure Database [ICSD 83791]). Clinopyroxene diffraction patterns were matched to a monoclinic symmetry with parameters of $a = 9.8172$, $b = 8.9954$, $c = 5.2796$ and $\alpha = 90°$, $\beta = 106°$, $\gamma = 90°$ (ICSD 81446). Anorthite diffraction patterns were matched to a triclinic symmetry with parameters of $a = 8.1732$, $b = 12.8583$, $c = 14.1703$ and $\alpha = 93.2°$, $\beta = 116°$, $\gamma = 91.2°$ (ICSD 63547). Apatite diffraction patterns were matched to a hexagonal symmetry with parameters of $a = 9.4555$, $b = 9.4555$, $c = 6.8836$ and $\alpha = 90°, \beta = 90°, \gamma = 120$ (ICSD 87679).

The Pb isotopic compositions and U/Pb ratios of apatites in 72417 were measured in situ using a CAMECA IMS1280 large geometry ion microprobe at the NordSIMS facility, Swedish Museum of Natural History, Stockholm, Sweden. The SIMS methodology closely followed the analytical description published elsewhere (Nemchin et al., 2021; Snape, Nemchin, Grange, et al., 2016). A duoplasmatron ion source generated a $^{16}O_2^-$ primary beam with a current of approximately 2 nA, which was projected through a 100 µm Köhler aperture to obtain a spot size of 10 µm. Prior to analysis, an ~15 × 15 µm rastered area was pre-sputtered for ~80 s to remove the gold coat and to minimize surface contamination. This was followed by automatic centering of the secondary ion beam in the 3000 µm field aperture and automatic centering of the magnetic field. The secondary ions were measured using four low-noise (<0.003 counts per second) Hamamatsu 4146 ion counting electron multipliers. Background counts for each channel were measured at regular intervals during the session and all signals were above 3× the background count rates. The four Pb isotopes (^{204}Pb, ^{206}Pb, ^{207}Pb, and ^{208}Pb) were measured simultaneously in separate electron multipliers, one of which was also used to measure secondary ion beam intensities in a mass-switching sequence that included $^{40}Ca_2{}^{31}P^{16}O_4^+$ (the apatite matrix peak), $^{238}U^+$, $^{232}Th^{16}O^+$, and $^{238}U^{16}O^+$. The mass spectrometer was operated at a nominal mass resolution of 4860 (M/ΔM), sufficient to separate Pb peaks from molecular interferences. Measured U/Pb ratios were calibrated against the 1160 Ma apatite reference material NW1 (Li et al., 2012), while differences in detector gains were monitored and corrected using repeated analyses of the USGS BCR-2G reference glass (Woodhead & Hergt, 2000).

In addition to the potential presence of terrestrial common lead, the effect of any lunar initial Pb component in the analyses was also considered. Given the extremely radiogenic nature of lunar Pb compositions, even small amounts of lunar initial lead can result in significantly older apparent $^{207}Pb/^{206}Pb$ ages. Two corrections were tested to obtain purely radiogenic Pb isotope compositions of the apatite grains (i.e., where $^{204}Pb/^{206}Pb = 0$). In theory, a mixture of both terrestrial common Pb and lunar initial Pb could be present; however, it is not possible to identify this. Therefore, the two corrections tested represent endmember situations where any non-radiogenic Pb represented 100% of either: (1) contamination with terrestrial common Pb, using the modern day terrestrial Pb compositions of Stacey and Kramers (1975); or (2) a lunar initial Pb component from a source with a range of $^{238}U/^{204}Pb$ ratios ($\mu = 450$–3000). The lunar initial Pb compositions were calculated based on the multiple stage model of Snape, Nemchin, Grange, et al. (2016), where the bulk silicate Moon evolved with a μ-value of 450 from Canyon Diablo Troilite Pb isotope compositions (Göpel et al., 1985) from 4500 Ma until 4376 Ma. After this first stage, a differentiation event led to the formation of separate mantle sources with distinct μ-values. Evolution of the Pb isotope composition in the source of 72417 was assumed to have continued until approximately 4350 Ma, when most Mg-suite rocks are thought to have formed (Borg et al., 2015; Gaffney et al., 2023; Shearer et al., 2023). The radiogenic $^{207}Pb/^{206}Pb$ ratios were then used to calculate ages assuming $^{235}U/^{238}U = 137.818$ (Hiess et al., 2012) and decay constant recommendations of Steiger and Jäger (1977). Results are given in Table 4.

RESULTS

Petrographic Observations

In thin section, the dunites are clearly cataclastic breccias composed mainly of olivine clasts in a very fine-grained matrix (Figure 1). Olivine clasts show a range of sizes, with the largest measuring 0.6–1.7 mm, in a matrix

TABLE 4. Pb and U isotope data for two SIMS spots on apatite in sample 72417. Full details of lunar initial Pb correction provided in methods section.

Grain	$^{204}Pb/^{206}Pb$	±σ %	$^{207}Pb/^{206}Pb$	±σ %	$^{208}Pb/^{206}Pb$	±σ %	Inverse concordia columns[a] $^{238}U/^{206}Pb$	±σ %	$^{207}Pb/^{206}Pb$	±σ %	Dates (Ma) $^{207}Pb/^{206}Pb$	±σ	$^{206}Pb/^{238}U$	±σ	U (ppm)	Pb (ppm)	Source μ	Lunar initial Pb comp. $^{204}Pb/^{206}Pb$	$^{207}Pb/^{206}Pb$	Corrected sample values $^{207}Pb/^{206}Pb$	±σ %	Date (Ma)	±σ
Apatite 1[b]	0.00110	37.8	0.429	2.2	0.091	5.0	1.461	21.1	0.420	2.5	3983	36	3361	578	851	856	450	0.03321	1.594	0.389	2.5	3866	77
																	1000	0.02901	1.610	0.382	2.6	3840	79
																	3000	0.01986	1.645	0.357	2.8	3738	86
Apatite 2	0.00039	100.0	0.404	3.9	0.243	4.5	1.159	33.1	0.401	4.0	3913	59	4012	1074	814	1146	450	0.03321	1.594	0.390	4.1	3871	123
																	1000	0.02901	1.610	0.388	4.1	3863	124
																	3000	0.01986	1.645	0.379	4.2	3830	128

[a]Terrestrial common Pb corrected.
[b]Analysis ID: Apatite 1, 72417-1_ap-multi-mono_20161202@1; Apatite 2, 72417-1_ap-multi-mono_20161202@2.

of fine material of ~50–100 μm. Most clasts are angular, but a few have more rounded edges. Some show undulose extinction, mosaicism, and fractures that terminate at grain edges. The latter are probably the "irregular fractures" described by Snee and Ahrens (1975), who attributed them to impact shock. Minor minerals include anorthite, clinopyroxene, Cr-spinel, orthopyroxene, apatite, and rare Fe-Ni metal. Anorthite occurs as fine-grained inclusions in most of the olivine clasts. It is unevenly distributed, with some clasts displaying anorthite inclusions throughout the entire clast, while others have anorthite inclusions only in parts. Clinopyroxene occurs as rare separate clasts, usually with Cr-spinel and occasionally orthopyroxene, and as small inclusions in olivine. Both 72415 and 72417 contain apatite, which encloses the other minerals and thus appears to be late stage.

Clasts showing a variety of symplectite textures are distributed randomly through the breccia. These

FIGURE 1. Optical microscopy of part of thin section 72415,53 in (a) plane polarized light and (b) crossed polars. Scale bar is 1 mm.

symplectites vary in size, mineral associations, and relative abundances. The different textures are apparent in BSE and false-color X-ray maps (Figures 2–4, and Figures S4–S6). One common symplectite (referred to here as "type A") consists of single relatively large (100–300 μm diameter) olivine-free clasts composed of clusters of Cr-spinel + diopside ± enstatite ± Fe-Ni metal (Figure 2). Cr-spinel has a strong vermicular texture with elongate branches. Type B symplectites are formed of clusters of Cr-spinel and anorthite and are strongly associated with olivine (Figure 3a,b). The Cr-spinel is much less vermicular than in type A and instead forms blocky and elongate crystals, some of which contain Fe-Ni metal. A much smaller type of symplectite (type C) is only found inside olivine clasts where it forms abundant inclusions of strongly vermicular Cr-spinel + diopside ± enstatite. These intergrowths are only ~30 μm in size (Figure 3c,d). These "micro-symplectite inclusions" were considered by Bell et al. (1975) to have been former garnets. A fourth type (type D) is composed of intergrowths of Cr-spinel and diopside and is found only on the edges of olivine clasts where they have deeply indented margins and arm-like extensions in the host olivine (Figure 3e,f). Finally, Cr-spinel also appears with clinopyroxene as narrow linear vein-like features, which cross-cut some olivine clasts (Figure 4a,b). Some of these veins are tapered, and small symplectites have crystallized from them.

The relative abundances of the four types of symplectites varies considerably. Micro-symplectites (type C) are the most common, but their concentration varies from a few olivine clasts with a small number of symplectites to several with much high concentrations. The larger type A and type B structures occur in approximately equal abundance, whereas type D structures and veins are the least common.

A few other clasts are notable. One is composed of clinopyroxene, anorthite, Cr-spinel, olivine, and Fe, Ni-metal (Figure 4c,d). In CT scans, this type of fragment appears to be type B. Another clast shows an intergrowth of orthopyroxene, surrounded by clinopyroxene, in turn surrounded by anorthite (Figure 4e,f). This appears to be a disequilibrium texture, indicating a reaction of orthopyroxene being replaced by clinopyroxene, with anorthite crystallizing after clinopyroxene. Again, this may be a section through a type B structure, but one which failed to cut through Cr-spinel.

Detailed BSE and X-ray images reveal that many olivine clasts are crossed by bands of inclusions (Figure 5) consisting of anorthite and clinopyroxene, with very small crystals of Cr-spinel and iron metal. These inclusions were not mentioned in previous descriptions of 72415-7, but it is possible that they contributed to the olivine "igneous zonation" reported by Ryder (1992). Rare apatite forms anhedral crystals which occur along cracks, as larger blebs within olivine clasts, and enclosing parts of the fine-grained olivine matrix (Figure 6).

Micro-CT Images

Micro-CT images of the interiors of the dunite fragments in 3-D confirmed that Cr-spinel occurs in several different textural types of varying size and shape. Type A spinel–pyroxene clusters are single ellipsoidal (up to 0.3 mm diameter) grains of pyroxene intergrown with randomly orientated, highly vermicular Cr-spinel (Figure 7). Cr-spinel branches are in contact with each other and thus form a single crystal. These individual clusters generally have rounded edges but can have angular margins, indicating that they have been fractured. Type B anorthite-rich clusters are also ellipsoidal structures, larger than type A, being 1.2 mm long and 0.8 mm wide, with complex intergrowths with blocky or elongate Cr-spinel (Figure 7). Many Cr-spinel crystals form linear (rod-like) features which display a weak parallel orientation and often terminate in highly elliptical and flat plate-like structures. Since 2-D slice CT images replicate BSE images, a search was made for textures observed in thin section 72415,53 in individual CT slices of 72415_4. The blocky blebs, which are clearly cross-sections of Cr-spinel which run through large olivines in rod-like forms, can be identified in 2-D slices (Figure 8). Type C spinel–pyroxene inclusions inside olivine clasts cannot be easily imaged by CT scanning because of their small size. However, 2-D slice images show small high-density Cr-spinel inclusions randomly distributed in olivine clasts (Figure 8). Type D Cr-spinel symplectites were also too small to be imaged by CT but appear as bright specks in 2-D slices.

Electron Backscatter Diffraction

Electron backscatter diffraction data for sample 72415,53 show contrasting internal structures in the olivine clasts (Figure 9). One prominent granular olivine clast has no discernible preferred orientation, with each neighboring subgrains displaying distinct orientations. This texture indicates recrystallization and is consistent with mosaicism or fragmentation produced by shock pressures >50 GPa (Stöffler et al., 2017). Other clasts display evidence of partial recrystallization, with numerous crystallites, with each neighboring crystallite displaying different orientations. A third population of olivine clasts is unaltered and undeformed with little to no internal misorientation.

Sample 72417,1 displays a similar complex history, with olivine occurring both as undeformed clasts with

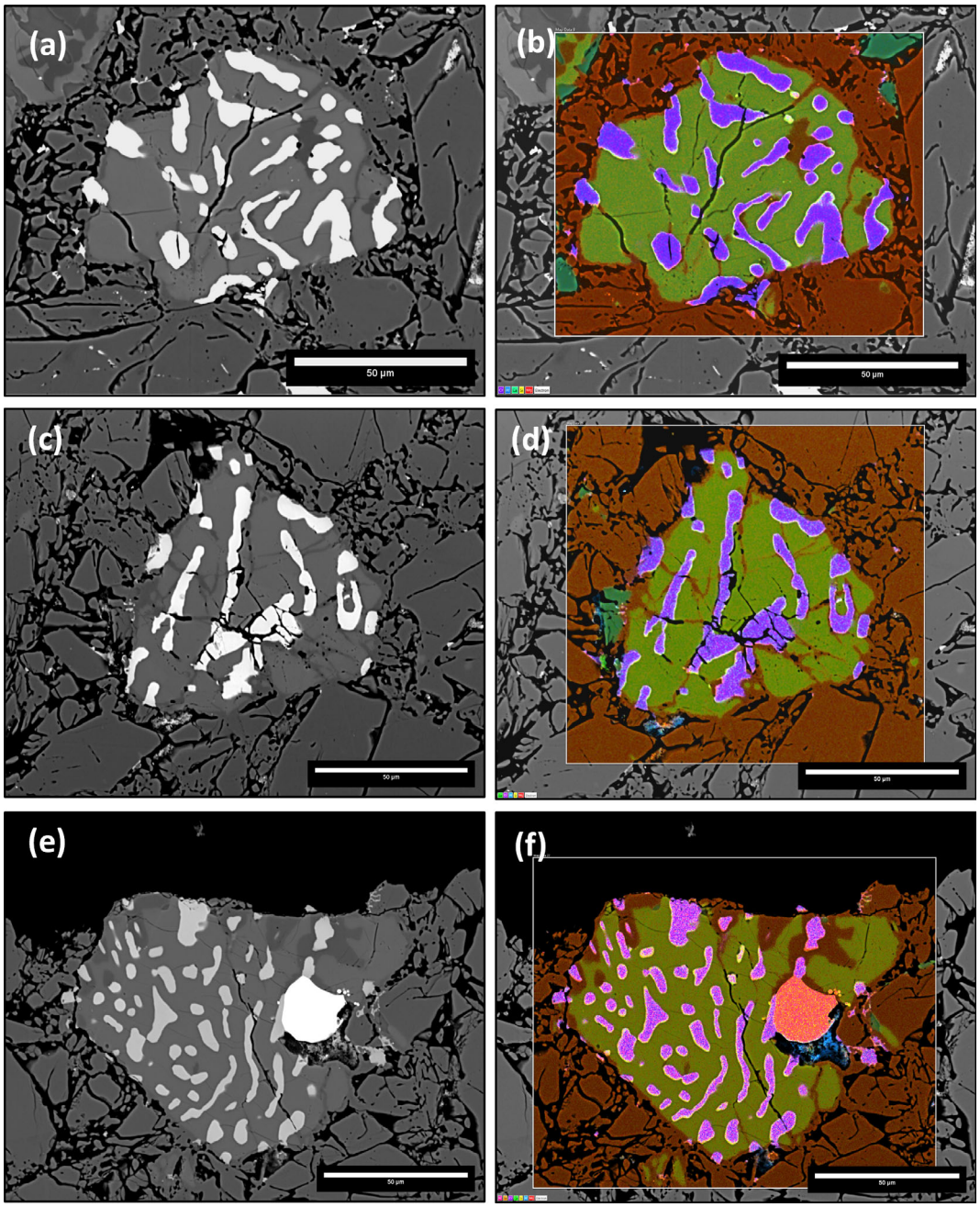

FIGURE 2. (a) BSE image from lunar dunite 72415,53, soi 14 (grid ref: Q19) showing a spinel-pyroxene cluster (type A) texture composed of spinel (white), diopside (light grey), enstatite (dark grey) surrounded by olivine (grey). Scalebar = 50 µm; (b) X-ray map from lunar dunite 72415,53, soi 14 (grid ref: Q19) showing a spinel-pyroxene cluster (type A) texture; Cr-spinel (purple), diopside (green) and enstatite (dark brown) Scalebar = 50 µm. (c) BSE image from lunar dunite 72415,53, soi G (grid ref: P21) showing a spinel-pyroxene cluster (type A) texture composed of Cr-spinel (white), diopside (light grey), enstatite (dark grey) surrounded by olivine (grey). Scalebar = 50 µm; (d) X-ray map from lunar dunite 72415,53, soi G (grid ref: P21) showing a spinel-pyroxene cluster (type A) texture; Spinel (purple) and diopside (green). Scalebar = 50 µm. (e) BSE image from lunar dunite 72415,53, soi 5 (grid ref: A25) showing a spinel-pyroxene cluster (type A) texture composed of Cr-spinel (white), diopside (light grey), enstatite (dark grey) surrounded by olivine (grey). Scalebar = 50 µm; (f) X-ray map from lunar dunite 72415,53, soi 5 (grid ref: A25) showing a spinel-pyroxene cluster (type A) texture; Cr-spinel (pink), diopside (green) and Fe-Ni metal (bright orange). Scalebar = 50 µm.

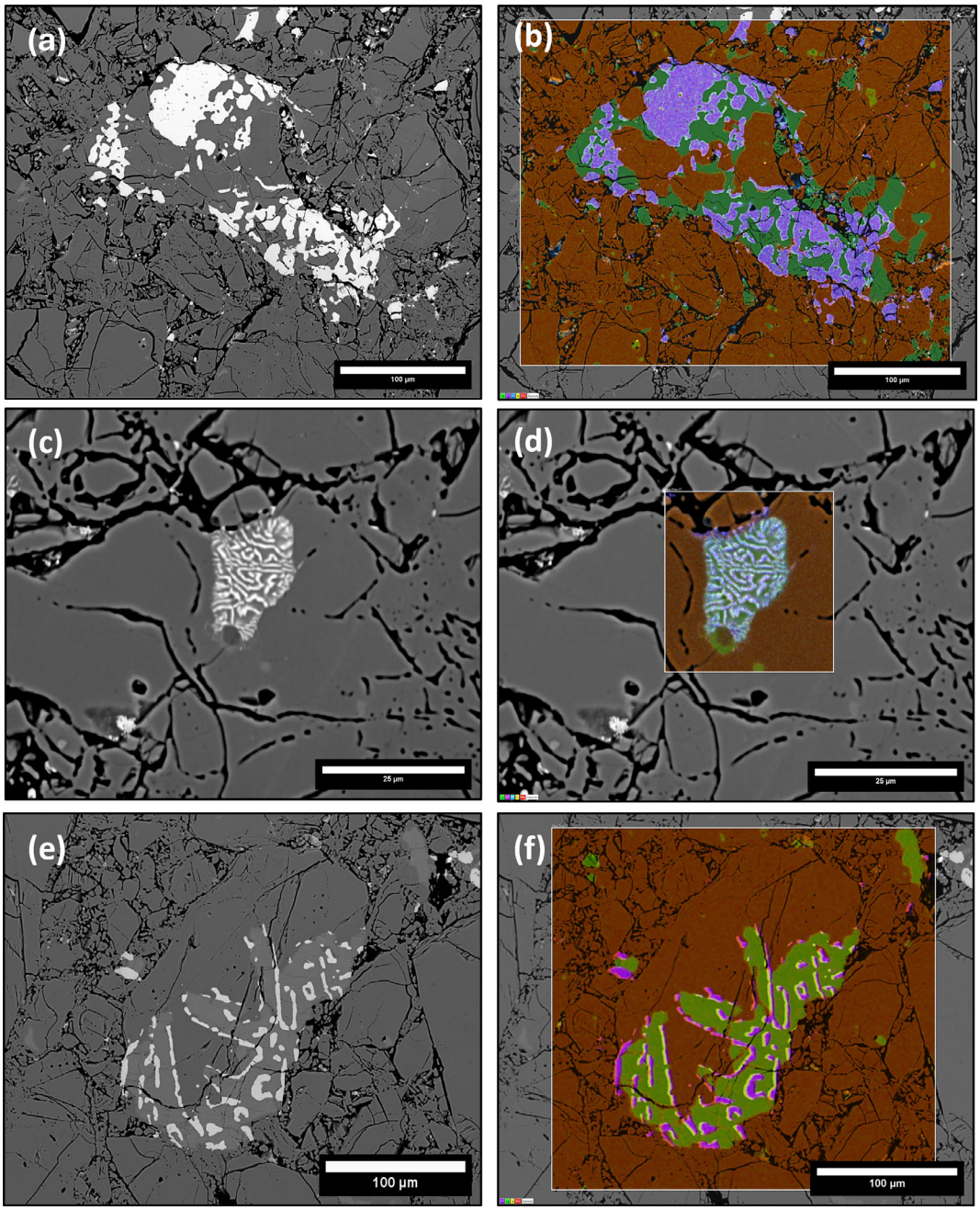

FIGURE 3. (a) BSE image from lunar dunite 72415,53, soi B (grid ref: C26, 27) showing a type B intergrowth, composed of Cr-spinel enclosed in anorthite. Scalebar = 100 µm; (b) X-ray map from lunar dunite 72415,53, soi B (grid ref: C26, 27) type B intergrowth, composed of Cr-spinel (purple) enclosed in anorthite (dark green). Scalebar = 100 µm. (c) BSE image from lunar dunite 72415,53 showing a type C symplectite composed of Cr-spinel (bright in BSE and diopside (light grey), enclosed in an olivine clast. Scalebar = 25 µm; (d) X-ray map from lunar dunite 72415,53, showing a type C symplectite composed of Cr-spinel (pale blue) and diopside (green), enclosed in an olivine clast. Scalebar = 25 µm. (e) BSE image from lunar dunite 72415,53, soi 3 (grid ref: C23,24) showing a type D structure on the rim of an olivine clast. Texture composed of spinel (white) and diopside (light grey). Scalebar = 100 µm; (f) X-ray map from lunar dunite 72415,53, soi 3 (grid ref: C23,24) showing a showing a type D structure on the rim of an olivine clast. Cr-spinel (purple) and diopside (green) Scalebar = 100 µm.

little to no internal misorientation and as those displaying evidence of recrystallization. Within a pocket of fine-grained matrix olivine with differing orientations, a crystal of apatite with a single orientation encloses the clasts (Figure 10). This confirms that the apatite is younger than the

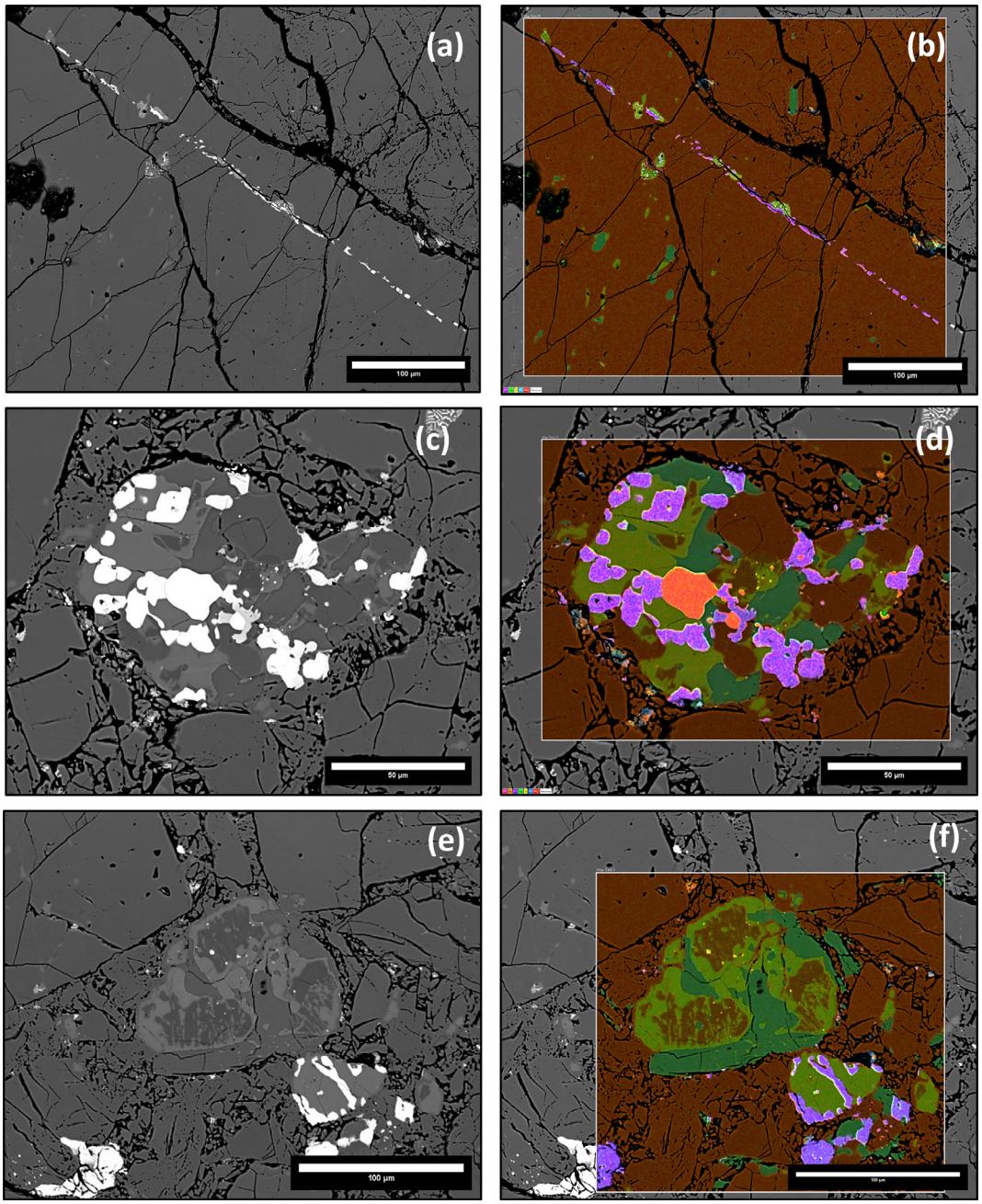

FIGURE 4. (a) BSE image from lunar dunite 72415,53, soi 6 (grid ref: K11, L11 and L12) showing a narrow linear feature (planar in CT scans), composed of Cr-spinel (white), cutting through olivine (grey) with rare cpx and anorthite inclusions. Scalebar = 100 μm; (b) X-ray map from lunar dunite 72415,53, soi 6 (grid ref: K11, L11 and L12) narrow linear feature (planar in CT scans), composed of Cr-spinel (purple), cutting through olivine (brick red) with rare cpx (green) and anorthite (dark green) inclusions. Scalebar = 100 μm. (c) BSE image from lunar dunite 72415,53, soi C, (grid ref: D22, 23) showing a clast composed of cpx, anorthite, Cr-spinel, and olivine. Bright grain in image is Fe-Ni metal. Scale bar is 50 μm. (d) X-ray map from lunar dunite 72415,53, (grid ref: D22, 23) showing a clast composed of cpx, anorthite, Cr-spinel, and olivine. Bright grain in image is Fe-Ni metal. (e) BSE image from lunar dunite 72415,53 X-ray map from lunar dunite 72415,53, soi 8a (grid ref: Q20) showing a showing a Cr-spinel-free clast consisting of an opx core, surrounded by cpx, in turn surrounded by anorthite, surrounded by other clasts of olivine. A type A symplectite fragment appears in the lower right of the image. Scalebar = 100 μm. (f) X-ray map from lunar dunite 72415,53, soi 8a (grid ref: Q20) showing a showing a Cr-spinel-free clast consisting of an opx core (brown), surrounded by cpx (green), in turn surrounded by anorthite (dark green), surrounded by other clasts of olivine (brick red). A type A symplectite fragment appears in the lower right of the image. Scalebar = 100 μm.

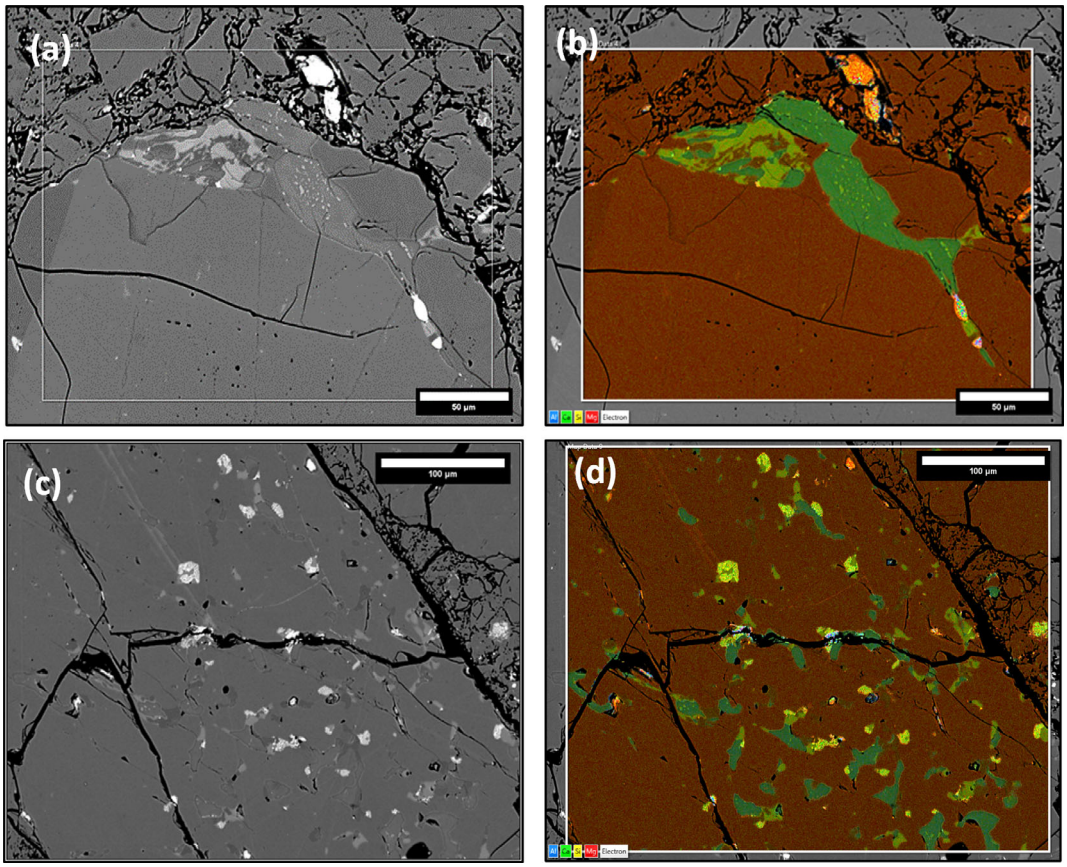

FIGURE 5. (a), BSE image from lunar dunite 72415,53, soi NHM 3a (grid ref: D14, 15, E24, 15) of an olivine clast with complex mixture of orthopyroxene, clinopyroxene, and anorthite, with anorthite apparently cutting the olivine. Scale bar is 50 μm. (b) X-ray map from lunar dunite 72415,53, soi NHM 3a (grid ref: D14, 15, E24, 15) of an olivine clast with complex mixture of opx (brown), cpx (pale green), and anorthite (dark green), with anorthite apparently cutting the olivine (brick red). Scale bar = 100 μm. (c) BSE image map of 72415,53, showing inclusions of anorthite, cpx and Cr-spinel inside olivine. Scale bar = 100 μm. (d) X-ray map of sample 72415,53, showing inclusions of anorthite (dark green), cpx (pale green), and Cr-spinel (yellow) inside olivine (brick red). Scale bar = 100 μm.

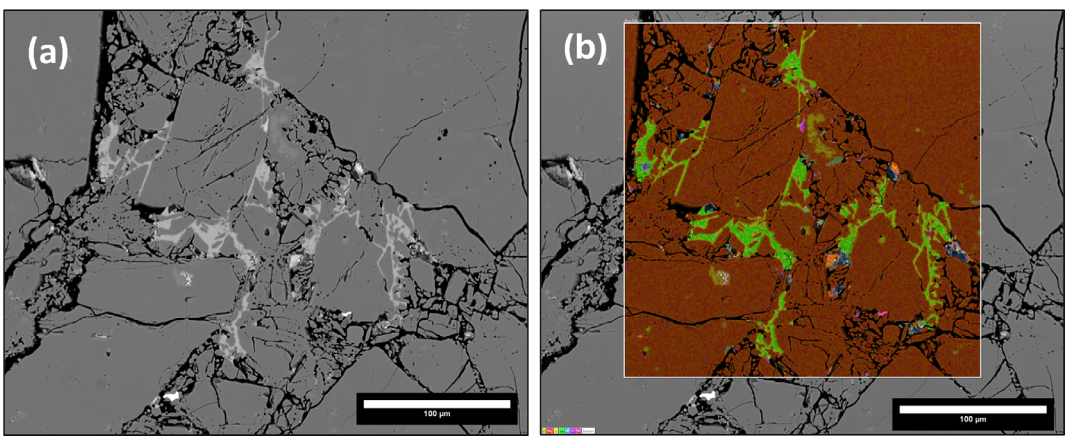

FIGURE 6. BSE image (a) and false-colored X-ray image (b) of apatite enclosing olivine (brick red) in 72415,53. Apatite is pale in BSE and green in the X-ray map. Scale bar is 100 μm.

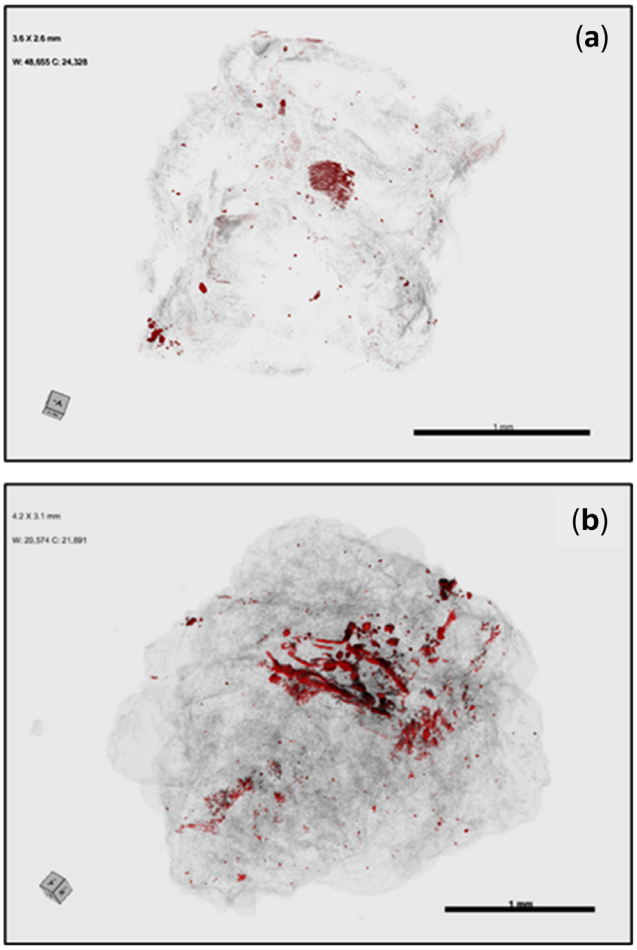

FIGURE 7. CT scan of fragment 72417-9003. (a) A type A Cr-spinel pyroxene cluster and (b) a type B Cr-spinel symplectite. Cr-spinel is red in both images. All other minerals are rendered transparent. Scale bar for both images = 1 mm. Movies of these images are available at https://www.youtube.com/channel/UCiR0Gr0pJpJExY7LXN5DNjg/.

brecciating event. Additionally, apatite appears to cross-cut olivine clasts or run along cracks, strengthening the argument for a secondary origin (Figure 10).

Mineral Compositions

Tables 1 and 2 show the variation in Cr-spinel composition in 72415,53 and 72417,1 according to their occurrence. Variations occur in Cr_2O_3 and Al_2O_3 contents, with Cr-spinel in type A clusters being Cr-rich (average Cr# = 67.3, where Cr# = 100 x atomic Cr/(Cr + Al)) and type B intergrowths showing a wide variation (Cr# = 48.8–69.8). Cr-spinels in type D rim textures have Cr#s of 67, whereas those in the vein-like structures have the highest Cr#s (75). Figure 11 shows the variation in Cr# and Mg# in Cr-spinels in a variety of clasts, together with those from troctolite 76535, which was considered by Schmitt (2016) to also have an origin as garnet. Analyses of Cr-spinel in type C microsymplectites were suspect due to overlap from the surrounding silicates and are not presented.

Anorthite ranges from An_{89} to An_{95} (Table 1). Clinopyroxene shows ranges of $Wo_{44-46}En_{49-54}Fs_{4.1-5.6}$, while orthopyroxene is $Wo_{2-3}En_{86-87}Fs_{10-11}$; both are similar to those reported by Meyer (2011). The fluorapatite contains 56.0 wt% CaO, 37.0 wt% P_2O_5, and 3.8 wt% F, in agreement with Dymek et al. (1975), and resembles lunar apatites discussed by Boyce et al. (2014).

All olivines have the same Mg# (100 × atomic Mg/[Mg + Fe]) of 87.4 ± 0.5 (Table 1), regardless of the type of clast in which they occur. Ryder (1992) analyzed olivine clasts in thin sections 74215,27 and 74215,28 and reported that the olivine compositions varied across individual clasts from 10.5 to 12.5 wt% FeO. This was interpreted as igneous zoning, although since each olivine clast was broken, the direction of zoning was ambiguous (i.e., cores and rims could not be identified). In contrast, the results of the present study show very little variation in FeO content in any single olivine clast, with all points in one clast yielding a mean and 1σ value of 11.53 ± 0.11 wt% FeO. This lack of detectable chemical zoning has been confirmed by WDS X-ray mapping of several olivine clasts. Thus, the results of this study contrast strongly with those of Ryder (1992) who concluded that the dunite shows igneous zoning and therefore crystallized at shallow pressures within the lunar crust. However, because the samples we have analyzed do not contain any coexisting minerals in equilibrium, no geothermobarometry estimates have yet been established. Ryder (1992) also reported that olivines contained up to 0.12 wt% CaO, which are similar to our results (Table 1).

Bulk Compositions of Type A Symplectite

The type A symplectite shown in Figure 2a consists of 72.2% clinopyroxene, 24.3% Cr-spinel, and a small amount (3.6%) of orthopyroxene with some fractures. Its average bulk composition was reconstructed from WDS data (Table 1) and given in Table 3. It is particularly rich in Cr_2O_3 (13 wt%) and CaO (16 wt%). The composition of the cluster can be accounted for by 64 wt% garnet and 31 wt% olivine, with a small fraction (5%) of excess SiO_2 remaining (Table 3). Assuming that the clusters were derived from a pure garnet and olivine mixture, the excess SiO_2 may result from minor patchy melt veining at and near the rim of this cluster, or minor analytical uncertainty. The reconstructed garnet consists of 64%

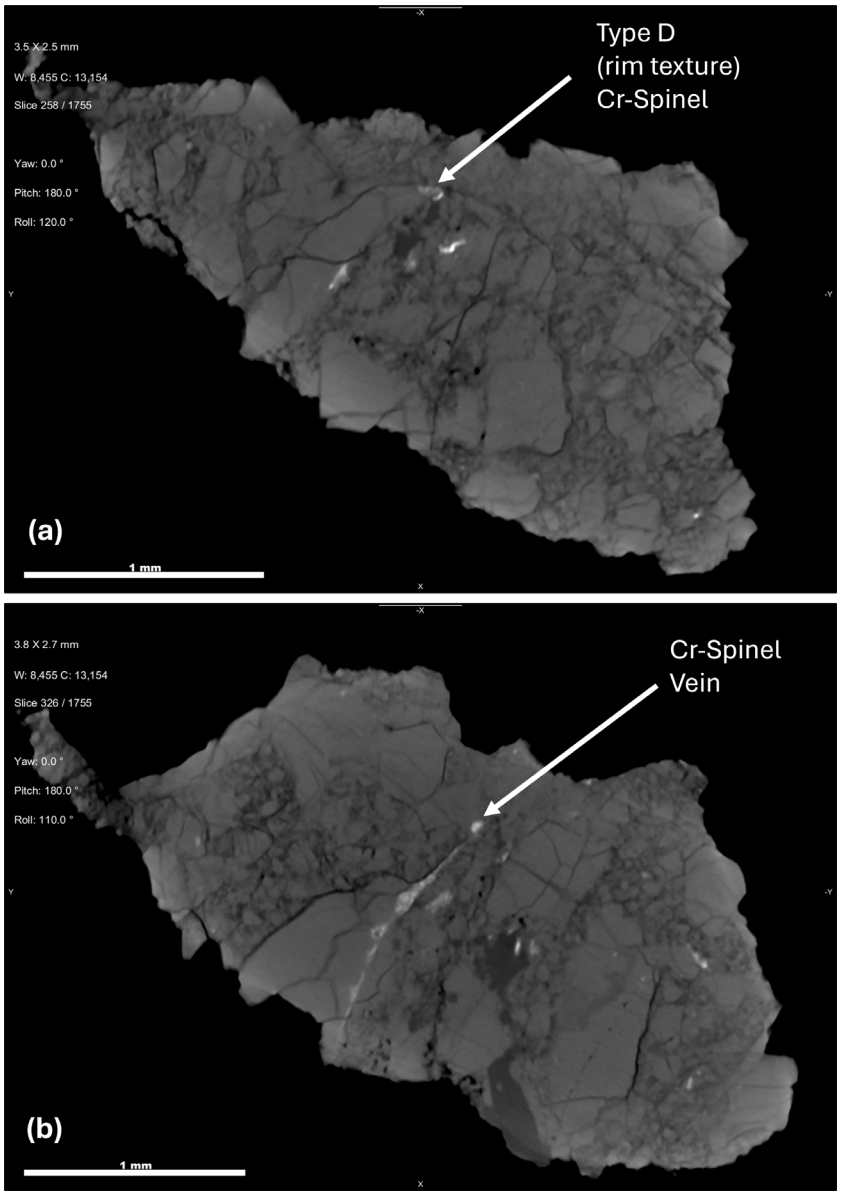

FIGURE 8. Two-dimensional images of 72417,9003, showing (a) type D Cr-spinel rim texture (white) and (b) vein of Cr-spinel (white). Scale bar = 1 mm.

uvarovite and 23% pyrope components, making it extremely Cr-rich. The cluster bulk composition, and so the reconstructed garnet and olivine, yields an Mg# = 82, whereas measured olivine in the sample has Mg# = 87. This difference between the Mg# of garnet and the Mg# of olivine is similar to that seen in garnets from terrestrial mantle xenoliths (McDonough & Rudnick, 1998).

Other type A inclusions have similar bulk compositions according to EDS rastered measurements, though with somewhat lower Cr_2O_3 and CaO contents (7–10 and 8–11 wt%, respectively). Interestingly, from EDS map data, the numerous type C microsymplectites appear to have similar bulk compositions to the type A symplectite analyzed above, containing similar average concentrations of Cr_2O_3 and CaO. This suggests a common origin for the type A and C symplectites, that is, garnet breakdown in equilibrium with olivine, and argues against the dehydrogenation redox mechanism suggested by Khisina et al. (2013) which presumably could not be responsible for the large and coarsely textured type A clusters. However, we note that the very high Cr content of the inferred garnets is difficult to explain. Conversely, type B inclusions have varied but noticeably different compositions, with much lower Cr_2O_3.

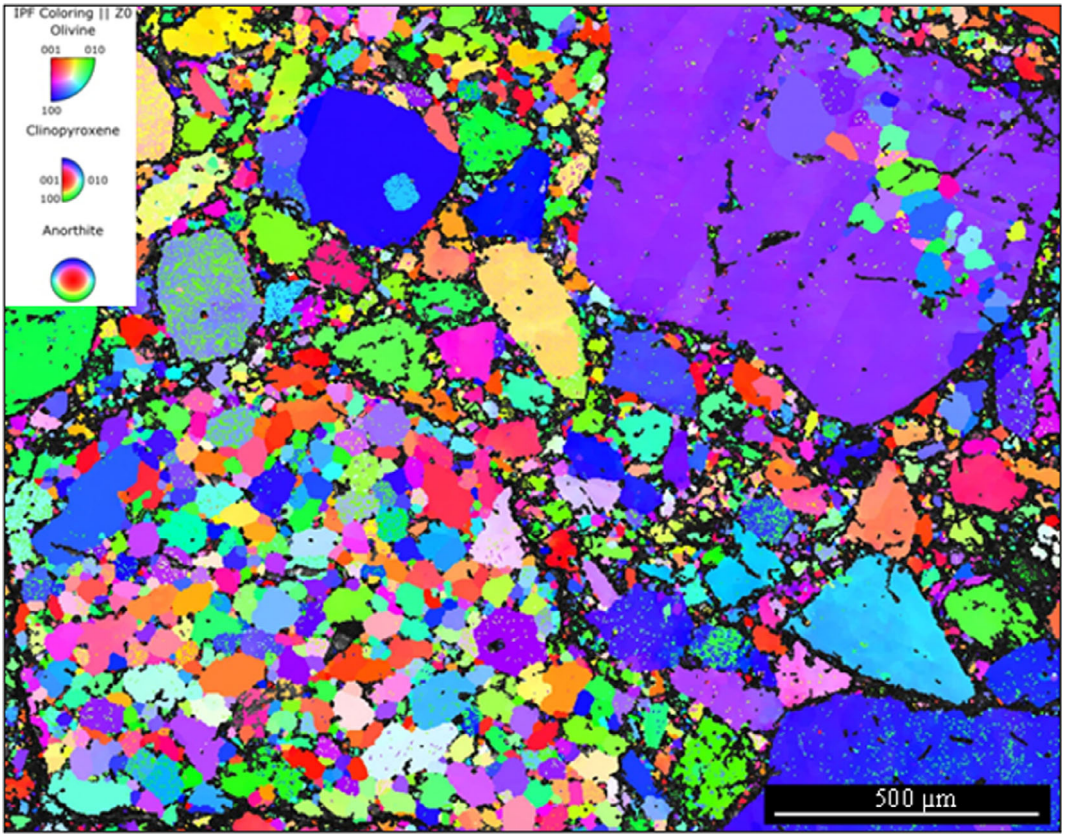

FIGURE 9. Inverse pole figure (IPF) map of sample 72415,53. Clasts display total recrystallization (bottom left), partial recrystallization (top right), and several clasts with no deformation nor evidence of recrystallization. Scale bar is 500 µm.

U–Pb Dating

Two apatite grains (Apatite_1 and _2) in 72417 were analyzed for their U-Th-Pb isotope compositions by SIMS. The terrestrial common Pb correction results in $^{207}Pb/^{206}Pb$ dates of 3983 ± 72 Ma and 3913 ± 118 Ma (2σ uncertainties). Correcting the Pb isotope compositions assuming a lunar initial Pb composition resulted in a range of $^{207}Pb/^{206}Pb$ dates of ~3740–3870 Ma for Apatite_1 and ~3830–3870 Ma for Apatite_2, with similar uncertainties to the common Pb-corrected dates. The youngest of these dates are extreme lower limits and are viewed as unlikely as they reflect incorporation of Pb that evolved in a source with extremely high μ-values (3000), similar to those inferred for KREEP (Snape, Nemchin, Bellucci, et al., 2016). More moderate source μ-values (450–1000) result in ages that are within uncertainty of the terrestrial common Pb-corrected dates. In all cases, the $^{207}Pb/^{206}Pb$ dates are concordant with the $^{206}Pb/^{238}U$ dates within the analytical uncertainties (Table 4).

DISCUSSION

The Search for Lunar Mantle Rocks

Dunites and other ultramafic rocks are of particular interest as possible samples of the lunar mantle (Moriarty III et al., 2021), and thus potentially as clues to the Moon's earliest differentiation and structure. They are very rare in the Apollo and Luna returned samples, and among lunar meteorites and their constituents. Apart from samples 72415–72417, dunites are known only as small clasts in Apollo breccias and lunar meteorites (Shearer, Burger, et al., 2015; Warren, 1993). Treiman and Semprich (2023) reported a dunite clast in a brecciated lunar meteorite NWA 11421. The clast consists of 95.3% olivine ($Fo_{83.5}$), 1.6% low-Ca pyroxene, 1.3% plagioclase, 1.1% augite, and 0.7% chromite, with the latter occurring as symplectites. Mineral thermobarometry gave an equilibration pressure of 0.4 GPa, so Treiman and Semprich (2023) considered it to be a piece of the lunar mantle. Sheikh et al. (2022)

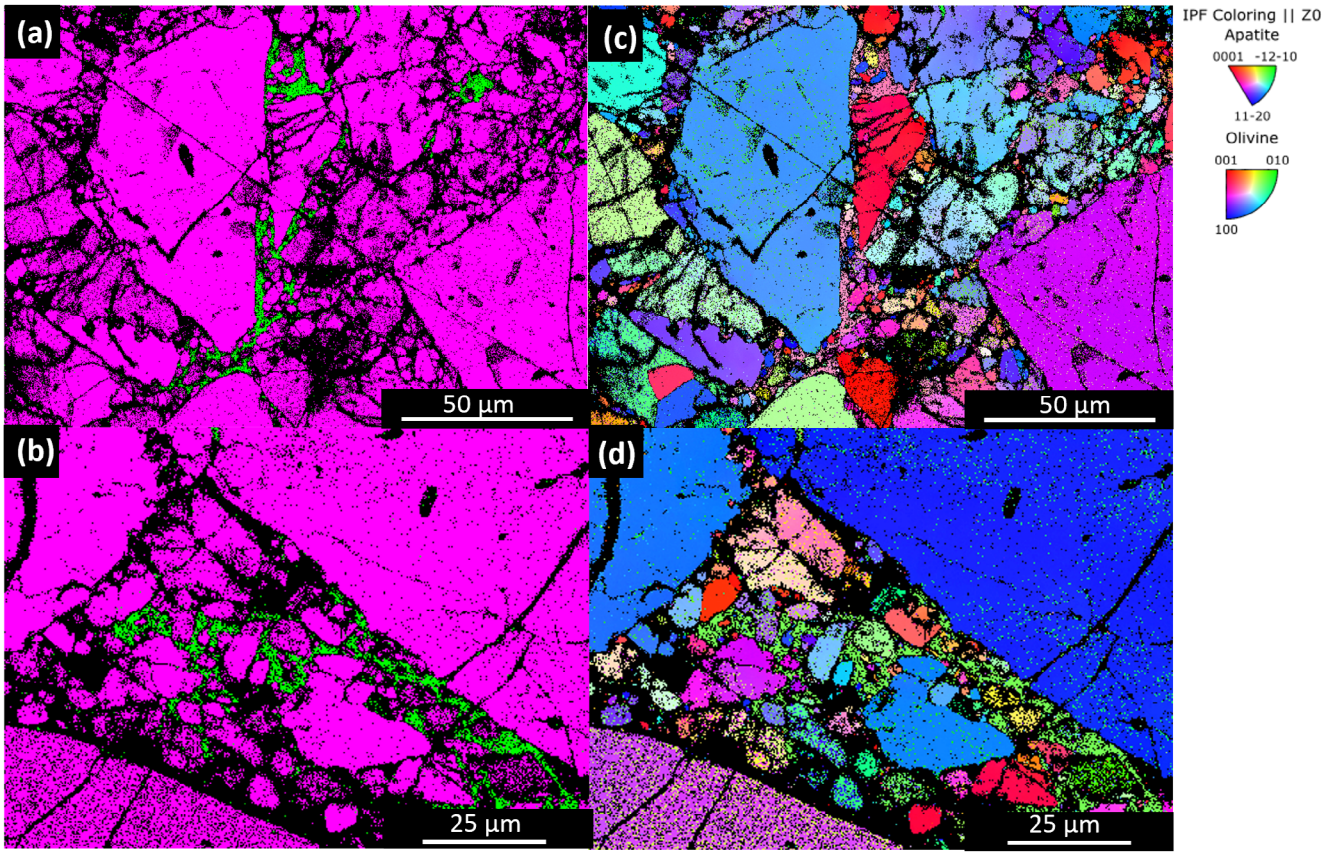

FIGURE 10. Phase maps (left) showing apatites in green and olivine clasts in purple. Inverse pole figures (IPF) (right) display the complexity of the olivine clasts within 72417, with differing orientations indicative of recrystallization or brecciation. The apatites encompassing the olivine clasts have a single orientation.

also described a dunite clast in lunar meteorite NWA 14900, with 99% olivine (Fo_{91}) and chromite (Cr# = 78–79), which might also be a piece of lunar mantle because of its unusual mineral compositions.

The search for fragments of the lunar mantle on the surface of the Moon has likewise yielded few positive results (Shearer, Burger, et al., 2015; Sun & Lucey, 2022), although data from the Grail and SELENE/Kaguya missions (Miljković et al., 2015; Yamamoto et al., 2010) have shown high Mg abundances surrounding most large (>200 km) lunar impact basins, interpreted as the presence of olivine of possible mantle origin. However, new material returned by Chang'e-6 may well contain fragments of the mantle excavated by the South Pole-Aitkin Basin impact (Jia et al., 2024; Zeng et al., 2023).

Geochronology and Origin of 72415-7

The age of the apatites in 72417 reported here is significantly younger than earlier reported ages of the Apollo 17 dunites. Papanastassiou and Wasserburg (1975) determined an Rb-Sr age of 4.55 ± 0.16 Ga for 72415 and Premo and Tatsumoto (1992) obtained similar ages by the U–Pb (4.52 ± 0.06 Ga) and Pb–Pb (4.37 ± 0.23 Ga) systems. Most of these ages are significantly older than those of the Mg-suite rocks, which typically have formation ages of ~4.35 Ga (Borg et al., 2015; Gaffney et al., 2023; Shearer et al., 2023). U–Pb analyses of two apatites in 72417 reported here (Table 4) yielded younger ages of 3983 ± 72 Ma and 3913 ± 118 Ma. Based on the microstructural data (Figure 10), these ages probably record the timing of impact or a secondary process after impact. The impact event that formed the Serenitatis Basin occurred at ~4.2 Ga (Černok et al., 2021), considerably older than these apatite ages. However, the age for the Imbrium impact at ~3.9 Ga (Nemchin et al., 2021; Zhang et al., 2019) is much closer to the ages presented here. Therefore, it is plausible that the Imbrium event was responsible for the brecciation, deformation, and apatite mobility in 72415-7 and also for transporting the rock to its final location in the Apollo 17 landing site. However, all basin formation ages are subject to debate, and the age of the Crisium impact also needs to be

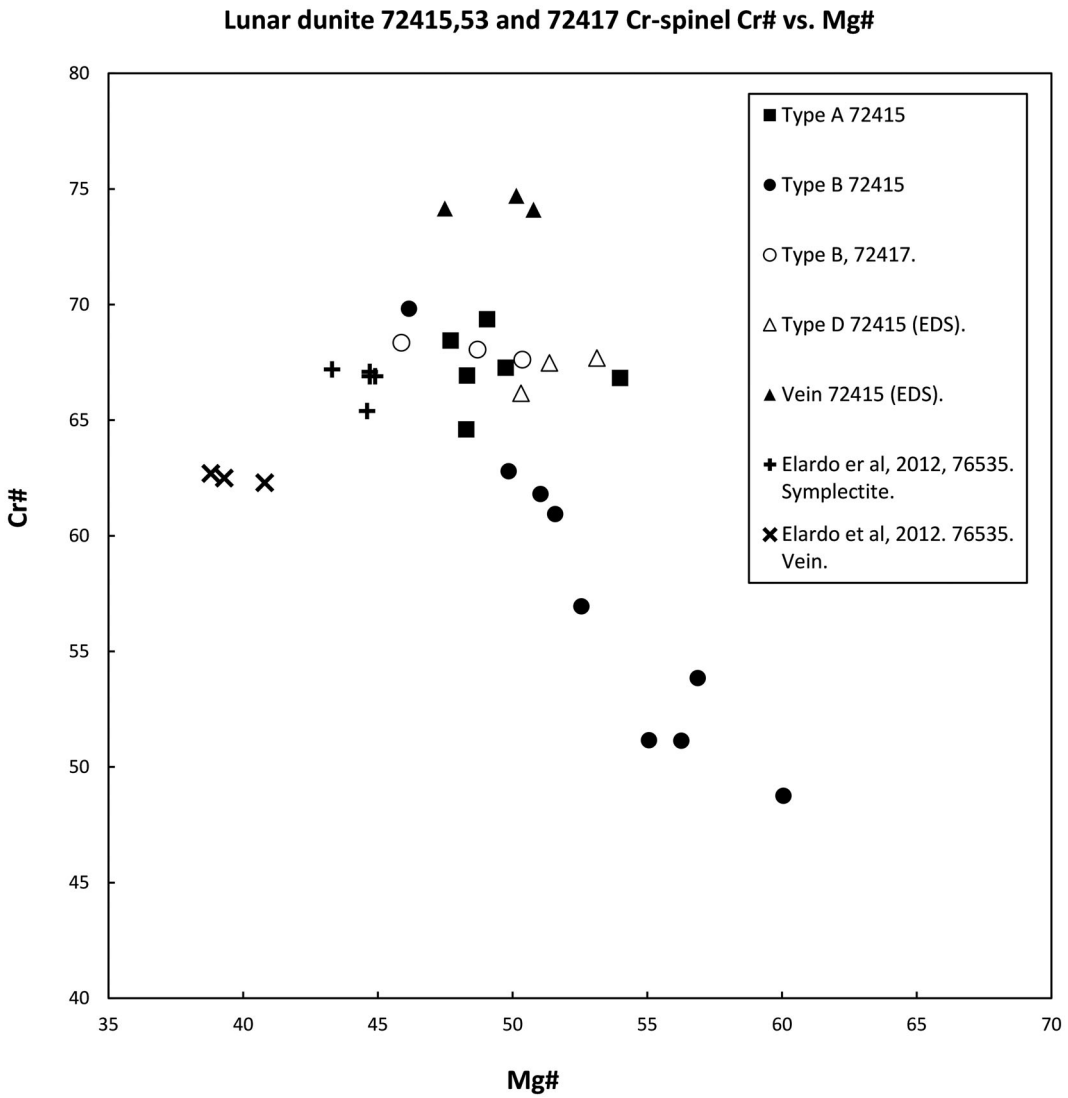

FIGURE 11. Mg# versus Cr# of different types of Cr-spinels analyzed by electron microprobe in 72415, 53, 72417,1, and 76535 (Elardo et al., 2012).

constrained. A reappraisal of the age of original crystallization of 72415-7 would be helpful in confirming the origin of these dunites.

The Imbrium excavation cavity is estimated to be 1160 km in diameter, and up to 80 km in maximum depth in a region with a maximum crustal thickness of 55 km (Spudis, 1993; Spudis et al., 1988). The EBSD evidence of shock metamorphism (Figure 9), in terms of partial and total recrystallization of olivine, can be attributed to a deep-excavating impact. Granular texture in olivine grains within angrite meteorites displays near-identical textures (Rider-Stokes et al., 2022) and has similarly been related to very large-scale impact events. Stöffler et al. (2017) suggested that melting and recrystallization can result from pressures >50 GPa. Thus, there is strong circumstantial evidence that these samples came from the lunar mantle.

Origin of Symplectites

Symplectites can form in several different ways, including magmatic co-crystallization, solid-melt reaction, pressure release, and metamorphic transformation (Elardo et al., 2012). Based on BSE images, elemental maps, 2-D and 3-D textures in CT, and EMPA data, the various occurrences of Cr-spinel in 72415-7 appear to have different origins. From their mineralogy, the anorthite-bearing symplectites (types B and D) are considered to be younger than the type A anorthite-free spinel–pyroxene clusters. A comparison with Mg-suite rocks (Elardo

et al., 2012) suggests some similarities and some differences for the textures observed in 72145-7. In particular, the veins of Cr-spinel that cut through olivine grains (Figure 4a,b) closely resemble chromite veins in Mg-suite troctolite 76535, which were interpreted as feeder channels for a Cr-, Fe-rich melt (Elardo et al., 2012). Type D symplectites, which appear on the margins of olivine grains, may be similar to the symplectites in Mg-suite rocks, which also always occur on grain boundaries, recording interaction with this external magma. These are therefore considered to have a magmatic or even metasomatic origin. However, there are some significant differences with Mg-suite rocks, including a complete lack of melt inclusions in 72415-7 (unless the inclusions identified in Figure 5c,d are crystallized melt). Furthermore, none of the symplectites in the Mg-suite resembles the type A spinel–pyroxene clusters in 72415-7.

Figure 12 shows the relative ages of each textural type of Cr-spinel symplectite and their proposed origins in the lunar interior. Cr-spinel in large olivine-free ellipsoidal clusters (type A) shows highly vermicular intergrowths with diopside and enstatite (Figures 2 and 7). This texture is identical to that of spinel–pyroxene clusters found in terrestrial mantle xenoliths (Mercier & Nicolas, 1975; Basu & Macgregor, 1976), visualized in 3-D by Bhanot et al. (2017). In the terrestrial mantle, such clusters are inferred to have formed by decompression and decomposition of garnet, the stable aluminous phase at pressures >1.3 GPa on Earth. Terrestrial spinel–pyroxene clusters formed by the following reaction (Kushiro & Yoder Jr, 1966; Green & Ringwood, 1967):

Olivine + Garnet ⇌ Diopside + Enstatite + Spinel.

This transformation would occur at depths of >400 km (>2.2 GPa) on the Moon. The estimated

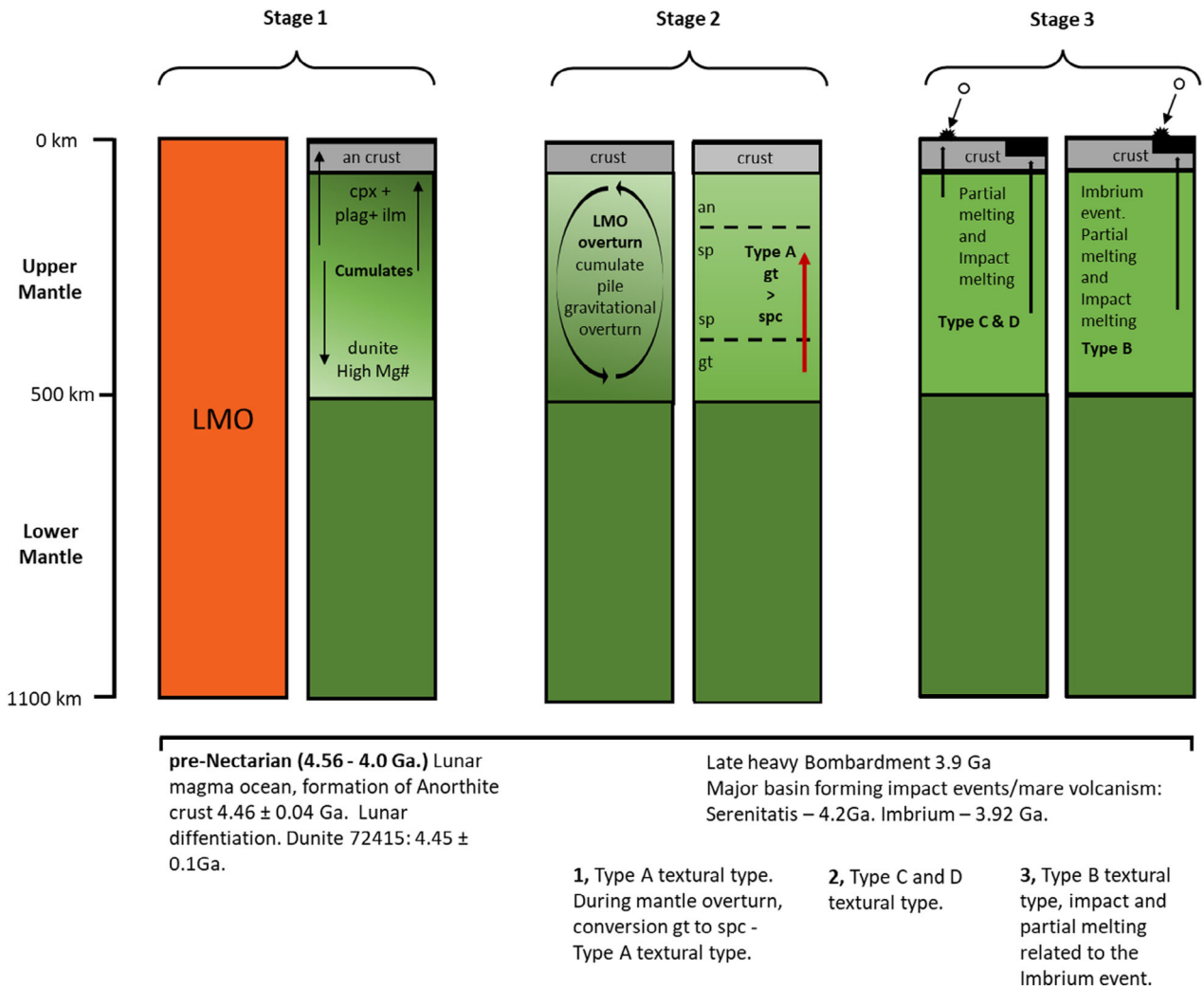

FIGURE 12. Proposed timeline for origin of dunites 72415–72417. An, anorthositic; cpx, clinopyroxene; gt, garnet; ilm, ilmenite; LMO, lunar magma ocean; ol, olivine; opx, orthopyroxene.

composition of the garnet is very unusual, being both Ca- and Cr- rich (Table 3). Although such compositions are not common for terrestrial mantle garnet, Cr- and Ca-rich garnets have been found in several locations on Earth where mantle rocks have been brought to the surface by kimberlite eruptions (Chepurov et al., 2017; Clarke & Carswell, 1977; Griffin et al., 1999; Sobolev et al., 1973). The origin of these terrestrial garnets is uncertain, but they are clearly present in the Earth's mantle, so their postulated presence in the lunar mantle is not entirely unlikely. Type A symplectites are always found separate from the other constituents of 72415-7, suggesting that they were a separate phase before their metamorphic transformation. This implies that the original garnet was isolated from the olivine, as occurs in terrestrial garnet peridotite xenoliths.

Garnet has been suggested to be present in the Moon's lower mantle by Neal (2001), Johnson et al. (2021), Jing et al. (2022), Kraettli et al. (2022), Borg and Gaffney (2023), and Wood et al. (2024), although no garnet has yet been found in a lunar sample. As discussed by Schmitt (2016), since the Moon lacks plate tectonics, mantle overturn provides the only possible mechanism to move garnet-bearing mantle into the spinel stability field to form type A Cr-spinel–pyroxene clusters. Mantle overturn, whether gravity-driven (Prissel et al., 2023) or impact-induced (Zhang et al., 2022), would have brought the dunite to a position beneath the lunar Moho, where it would have remained until excavated by impact. Schmitt (2016) suggested a depth of approximately 50 km. At this depth, anorthite would be stable, which explains the presence of numerous anorthite inclusions in many olivine clasts (Figure 5).

Type B symplectites are complex structures between Cr-spinel, anorthite, and olivine, all contained within large olivine clasts. They differ from type A symplectites in several ways. The Cr-spinel has a lower Cr# and forms less vermicular but blocky blebs. Anorthite also forms blocky linear grains and is associated with both olivine and Cr-spinel. Type B symplectites therefore have a much shallow origin in the anorthite stability field, perhaps formed via interaction between olivine and decompression melts. The variations in spinel chemistry in type B symplectites (Figure 11) imply a reaction with a lower Cr#, higher Mg# reservoir, such as olivine. As suggested by Dymek et al. (1975), these melts may have formed during basin-forming impacts.

Type C microsymplectites always occur inside olivine clasts. They are composed of Cr-spinel + anorthite ± diopside ± enstatite, and the 2-D CT slice images show that they are randomly distributed throughout the olivine clasts. Khisina et al. (2013) reported the presence of similar symplectite inclusions of chromite and diopside in olivine grains from lunar regolith collected by Luna-24. They attributed the inclusions to segregation of Cr and Ca from the host olivine. Formation of the inclusions was due to dehydrogenation of the olivine, because of decompression, which caused oxidation of Cr^{2+} to Cr^{3+} in the olivine. This caused Cr^{3+} to diffuse from the olivine, accompanied by Ca^{2+}, resulting in the intergrowth of Cr-rich spinel and Ca-rich pyroxene. Although Khisina et al. (2013) studied elongate lamellae, rather than the more spherical inclusions found in 72415, it may be that the same dehydrogenation process that formed the lamellae also formed the microsymplectites. However, the fact that they have a similar composition to the type A symplectites is puzzling, and further work is being undertaken to determine the mechanism of formation.

Type D symplectites are small lobate structures composed of Cr-spinel and diopside, always found on the rims of olivines (Figure 8). Thus, they are most likely to be reaction rim textures. Olivine clasts with these textures are often cut by large cracks. Thus, these symplectites probably also formed by interaction with melts caused by decompression or impact.

CONCLUSIONS

Apollo 17 lunar dunites 72415–72417 have been re-examined using a variety of modern petrological and geochemical techniques. Several different Cr-spinel textural types have been identified by EMPA and micro-CT. Each textural type is defined by its chemical composition and relationship with olivine and represents a different stage in the history of the dunites (Figure 12). The most significant in terms of petrogenesis are the large (100–300 μm diameter) ellipsoidal spinel–pyroxene clusters, which may have been formed by the metamorphic transformation of deep mantle Cr-rich garnet due to lunar mantle overturn. The dunite is therefore probably a fragment of the lunar mantle, initially formed by crystallization of the LMO, at depths corresponding to the pressure of the garnet peridotite facies (~2.2 GPa, ~420 km).

Microsymplectites of Cr-spinel associated with inclusions of clinopyroxene and anorthite were likely formed by dehydrogenation during decompression. These may account for the "igneous zoning" reported by Ryder (1992). Other features may have been formed by injection of silicate melt or reaction with silicate melt, either during overturn (decompression) or related to impact. Vein-like features formed of Cr-spinel and clinopyroxene may also relate to this event. Apatites yield ages of 3.9 Ga for their formation or remobilization, consistent with the age of the basin-forming Imbrium impact. We therefore suggest that the Imbrium impact may have been responsible for bringing the dunites from the shallow mantle to the lunar surface.

This study has also evaluated the severity of shock attributed to deep-excavating impacts on the Moon as being >50 GPa. This contrasts with the study of Ryder (1992) who suggested a shallow origin for the Apollo 17 dunites. We therefore agree with Bell et al. (1975) and Schmitt (2016) that these rocks represent lunar mantle material, brought up from depth by convective overturn to a location just beneath the crust–mantle boundary, and then excavated by impact.

Acknowledgments—We are grateful to Apollo astronaut Harrison Schmitt for collecting the sample and recognizing its potential significance; Ryan Ziegler (JSC, Houston) for providing fragments and thin sections; Brett Clark (CT scanning at the NHM, London); John Spratt (Electron microprobe at the NHM, London); Tobias Salge and Chiara Petrone (BSE and X-Ray mapping at NHM), Guilia Degli-Alessandrini (EBSD assistance at Open University), and Lee White (EBSD interpretations and discussions at Open University). The NordSIMS facility was funded by Swedish Research Council infrastructure grant 2017-00671 at the time of analysis. This is NordSIMS contribution 772. We also thank Allan Treiman and Tim Johnson for helpful reviews of the manuscript, and Harrison Schmitt and Daniel Sheikh for additional comments.

Data Availability Statement—Data available on request.

Editorial Handling—Dr. Jeffrey Plescia

REFERENCES

Albee, A. L., Dymek, R. F., and DePaolo, D. J. 1975. Spinel Symplectites: High-Pressure Solid-State Reaction or Late-Stage Magmatic Crystallization?. *6th Lunar and Planetary Science Conference*.

Basu, A. R., and MacGregor, I. D. 1976. Chromite spinels from ultramafic xenoliths. In *Chromium: its physicochemical behavior and petrologic significance*, 937–945. Pergamon.

Bell, P. M., Mao, H. K., Roedder, E., and Weiblen, P. W. 1975. The problem of the origin of symplectites in olivine-bearing lunar rocks. *Lunar and Planetary Science Conference Proceedings* 6: 231–248.

Bell, P. M., Mao, H. K., Roedder, E., and Weiblen, P. W. 1975. The Problem of the Origin of Symplectites in Olivine-Bearing Lunar Rocks. *6th Lunar and Planetary Science Conference*, pp. 231–48.

Bhanot, K. K., Downes, H., Petrone, C. M., and Humphreys-Williams, E. 2017. Textures in Spinel Peridotite Mantle Xenoliths Using Micro-CT Scanning: Examples from Canary Islands and France. *Lithos* 276: 90–102.

Borg, L. E., and Gaffney, A. 2023. A Deep Lunar Magma Ocean. 85th Meteoritical Society Conference, abstract #6237.

Borg, L. E., Gaffney, A. M., and Shearer, C. K. 2015. A Review of Lunar Chronology Revealing a Preponderance of 4.34-4.37 Ga Ages. *Meteoritics & Planetary Science* 50: 715–732.

Boyce, J. W., Tomlinson, S. M., McCubbin, F. M., Greenwood, J. P., and Treiman, A. H. 2014. The Lunar Apatite Paradox. *Science* 344: 400–402.

Černok, A., White, L. F., Anand, M., Tait, K. T., Darling, J. R., Whitehouse, M., Miljković, K., et al. 2021. Lunar Samples Record an Impact 4.2 Billion Years Ago that May Have Formed the Serenitatis Basin. *Nature Communications Earth & Environment* 2: 1–9.

Chepurov, A. A., Turkin, A. I., and Pokhilenko, N. P. 2017. Crystallization of High-Ca Chromium Garnet upon Interaction of Serpentine, Chromite, and Ca-Bearing Hydrous Fluid. *Doklady Earth Sciences* 476: 1229–32.

Clarke, D. B., and Carswell, D. A. 1977. Green Garnets from the Newlands Kimberlite, Cape Province, South Africa. *Earth and Planetary Science Letters* 34: 30–38.

Dymek, R. F., Albee, A. L., and Chodos, A. A. 1975. Comparative Petrology of Lunar Cumulate Rocks of Possible Primary Origin—Dunite 72415, Troctolite 76535, Norite 78235, and Anorthosite 62237. *6th Lunar and Planetary Science Conference*, pp. 301–41.

Elardo, S. M., McCubbin, F. M., and Shearer, C. K., Jr. 2012. Chromite Symplectites in Mg-Suite Troctolite 76535 as Evidence for Infiltration Metasomatism of a Lunar Layered Intrusion. *Geochimica et Cosmochimica Acta* 87: 154–177.

Gaffney, A. M., Gross, J., Borg, L. E., Hanna, K. L. D., Draper, D. S., Dygert, N., Elkins-Tanton, L. T., et al. 2023. Magmatic Evolution I: Initial Differentiation of the Moon. *Reviews in Mineralogy and Geochemistry* 89: 103–145.

Göpel, C., Manhes, G., and Allegre, C. J. 1985. U-Pb Systematics in Iron Meteorites—Uniformity of Primordial Lead. *Geochimica et Cosmochimica Acta* 49: 1681–95.

Green, D. H., and Ringwood, A. E. 1967. The Stability Fields of Aluminous Pyroxene Peridotite and Garnet Peridotite and their Relevance in Upper Mantle Structure. *Earth and Planetary Science Letters* 3: 151–160.

Griffin, W. L., Fisher, N. I., Friedman, J., Ryan, C. G., and O'Reilly, S. Y. 1999. Cr-Pyrope Garnets in the Lithospheric Mantle. I. Compositional Systematics and Relations to Tectonic Setting. *Journal of Petrology* 40: 679–704.

Hiess, J., Condon, D. J., McLean, N., and Noble, S. R. 2012. $^{238}U/^{235}U$ Systematics in Terrestrial Uranium-Bearing Minerals. *Science* 335: 1610–14.

Jia, Z., Chen, J., Kong, J., Qiao, L., Fu, X., and Ling, Z. 2024. Geologic Context of Chang'e-6 Candidate Landing Regions and Potential Non-mare Materials in the Returned Samples. *Icarus* 416: 116107.

Jing, J. J., Lin, Y., Knibbe, J. S., and van Westrenen, W. 2022. Garnet Stability in the Deep Lunar Mantle: Constraints on the Physics and Chemistry of the Interior of the Moon. *Earth and Planetary Science Letters* 584: 117491.

Johnson, T. E., Morrissey, L. J., Nemchin, A. A., Gardiner, N. J., and Snape, J. F. 2021. The Phases of the Moon: Modelling Crystallization of the Lunar Mantle Ocean through Equilibrium Thermodynamics. *Earth and Planetary Science Letters* 556: 116721.

Khisina, N. R., Wirth, R., Abart, R., Rhede, D., and Heinrich, W. 2013. Oriented chromite–diopside symplectic inclusions in olivine from lunar regolith delivered by "Luna-24" mission. *Geochimica et Cosmochimica Acta* 104: 84–98.

Kraettli, G., Schmidt, M. W., and Liebske, C. 2022. Fractional Crystallization of a Basal Lunar Magma

Ocean: A Dense Melt-Bearing Garnetite Layer above the Core? *Icarus* 371: 114699.
Kushiro, I., and Yoder, H. S., Jr. 1966. Anorthite—Forsterite and Anorthite—Enstatite Reactions and their Bearing on the Basalt—Eclogite Transformation. *Journal of Petrology* 7: 337–362.
Laul, J. C., and Schmitt, R. A. 1975. Dunite 72417-A Chemical Study and Interpretation. *6th Lunar and Planetary Science Conference*, pp. 1231–54.
Li, Q.-L., Li, X.-H., Wu, F.-Y., Yin, Q.-Z., Ye, H.-M., Liu, Y., Tang, G.-Q., and Zhang, C.-L. 2012. In-Situ SIMS U–Pb Dating of Phanerozoic Apatite with Low U and High Common Pb. *Gondwana Research* 21: 745–756.
McDonough, W. F., and Rudnick, R. L. 1998. Mineralogy and Composition of the Upper Mantle. *Reviews in Mineralogy* 37: 139–164.
Mercier, J. C., and Nicolas, A. 1975. Textures and Fabrics of Upper-Mantle Peridotites as Illustrated by Xenoliths from Basalts. *Journal of Petrology* 16: 454–487.
Meyer, C. 2011. Lunar Sample Compendium. http://www-curator.jsc.nasa.gov/.
Miljković, K., Wieczorek, M. A., Collins, G. S., Solomon, S. C., Smith, D. E., and Zuber, M. T. 2015. Excavation of the Lunar Mantle by Basin-Forming Impact Events on the Moon. *Earth and Planetary Science Letters* 409: 243–251.
Moriarty, D. P., III, Dygert, N., Valencia, S. N., Watkins, R. N., and Petro, N. E. 2021. The Search for Lunar Mantle Rocks Exposed on the Surface of the Moon. *Nature Communications* 12: 4659.
Neal, C. R. 2001. Interior of the Moon: The Presence of Garnet in the Primitive Deep Lunar Mantle. *Journal of Geophysical Research: Planets* 106(E11): 27865–85.
Nemchin, A. A., Long, T., Jolliff, B. L., Wan, Y., Snape, J. F., Zeigler, R., Grange, M. L., et al. 2021. Ages of Lunar Impact Breccias: Limits for Timing of the Imbrium Impact. *Geochemistry* 81: 125683.
Papanastassiou, D. A., and Wasserburg, G. J. 1975. Rb-Sr Study of a Lunar Dunite and Evidence for Early Lunar Differentiates. *6th Lunar and Planetary Science Conference*, pp. 1467–89.
Premo, W. R., and Tatsumoto, M. 1992. U-Pb Isotopes in Dunites 72415. *23rd Lunar and Planetary Science Conference*, p. 1103.
Prissel, T. C., Zhang, N., Jackson, C. R., and Li, H. 2023. Rapid Transition from Primary to Secondary Crust Building on the Moon Explained by Mantle Overturn. *Nature Communications* 14: 5002.
Rider-Stokes, B. G., Greenwood, R. C., Anand, M., White, L. F., Franchi, I. A., Debaille, V., Goderis, S., et al. 2022. Outward Displacement of Rocky Planetesimals in the Early Solar System. *Nature Astronomy* 7: 836–842. https://doi.org/10.1038/s41550-023-01968-0.
Ryder, G. 1992. Chemical Variation and Zoning of Olivine in Lunar Dunite 72415-Near-Surface Accumulation. *22nd Lunar and Planetary Science Conference*, pp. 373–80.
Schmitt, H. H. 2016. Symplectites in Dunite 72415 and Troctolite 76535 Indicate Mantle Overturn beneath Lunar near-Side. *47th Lunar and Planetary Science*, abstract #1903, p. 2339.
Shearer, C., Neal, C. R., Glotch, T. D., Prissel, T. C., Bell, A. S., Fernandes, V. A., Gaddis, L. R., et al. 2023. Magmatic Evolution II: A New View of Post-Differentiation Magmatism. *Reviews in Mineralogy and Geochemistry* 89: 147–206.
Shearer, C. K., Burger, P. V., Bell, A. S., Guan, Y., and Neal, C. R. 2015. Exploring the Moon's Surface for Remnants of the Lunar Mantle 1. Dunite Xenoliths in Mare Basalts. A Crustal or Mantle Origin? *Meteoritics & Planetary Science* 50: 1449–67.
Shearer, C. K., Elardo, S. M., Petro, N. E., Borg, L. E., and McCubbin, F. M. 2015. Origin of the Lunar Highlands Mg-Suite: An Integrated Petrology, Geochemistry, Chronology, and Remote Sensing Perspective. *American Mineralogist* 100: 294–325.
Sheikh, D., Ruzicka, A. M., Hutson, M. L., and Stream, M. 2022. Dunite Clast in Lunar Meteorite Northwest Africa (NWA) 14900: Mantle Derived?.
Snape, J. F., Nemchin, A. A., Bellucci, J. J., Whitehouse, M. J., Tartèse, R., Barnes, J. J., Anand, M., Crawford, I. A., and Joy, K. H. 2016. Lunar Basalt Chronology, Mantle Differentiation and Implications for Determining the Age of the Moon. *Earth and Planetary Science Letters* 451: 149–158.
Snape, J. F., Nemchin, A. A., Grange, M. L., Bellucci, J. J., Thiessen, F., and Whitehouse, M. J. 2016. Phosphate Ages in Apollo 14 Breccias: Resolving Multiple Impact Events with High Precision U-Pb SIMS Analyses. *Geochimica et Cosmochimica Acta* 174: 13–29.
Snee, L. W., and Ahrens, T. J. 1975. Shock-Induced Deformation Features in Terrestrial Peridotite and Lunar Dunite. *6th Lunar and Planetary Science Conference*, pp. 833–42.
Sobolev, N. V., Lavrent'ev, Y. G., Pokhilenko, N. P., and Usova, L. V. 1973. Chrome-Rich Garnets from the Kimberlites of Yakutia and their Parageneses. *Contributions to Mineralogy and Petrology* 40: 39–52.
Spudis, P. D. 1993. *The Geology of Multi-Ring Impact Basins*. Cambridge, UK: Cambridge University Press.
Spudis, P. D., Hawke, B. R., and Lucey, P. G. 1988. Materials and Formation of the Imbrium Basin. *18th Lunar and Planetary Science Conference*, pp. 155–68.
Stacey, J. S., and Kramers, J. D. 1975. Approximation of Terrestrial Lead Isotope Evolution by a Two-Stage Model. *Earth and Planetary Science Letters* 26: 207–221.
Steiger, R. H., and Jäger, E. 1977. Subcommission on geochronology: convention on the use of decay constants in geo-and cosmochronology. *Earth and planetary science letters* 36: 359–362.
Stöffler, D., Hamann, C., and Metzler, K. 2017. Shock Metamorphism of Planetary Silicate Rocks and Sediments: Proposal for an Updated Classification System. *Meteoritics and Planetary Science* 53: 5–49.
Sun, L., and Lucey, P. 2022. Searching for Mg-Rich Dunite Boulders on Lunar Surface and Implications to Mantle Compositions. LPI Contributions 2678, 1904.
Treiman, A. H., and Semprich, J. 2023. A Dunite Fragment in Meteorite Northwest Africa (NWA) 11421: A Piece of the Moon's Mantle. *American Mineralogist* 108: 2182–92.
Warren, P. H. 1993. A Concise Compilation of Petrologic Information on Possibly Pristine Non-Mare Moon Rocks. *American Mineralogist* 78: 360–376.
Wood, M. C., Gréaux, S., Kono, Y., Kakizawa, S., Ishikawa, Y., Inoué, S., Kuwahara, H., Higo, Y., Tsujino, N., and Irifune, T. 2024. Sound Velocities in Lunar Mantle Aggregates at Simultaneous High Pressures and Temperatures: Implications for the Presence of Garnet in the Deep Lunar Interior. *Earth and Planetary Science Letters* 641: 118792.
Woodhead, J., and Hergt, J. M. 2000. Pb-Isotope Analyses of USGS Reference Materials. *Geostandards Newsletter* 24: 33–38.

Yamamoto, S., Nakamura, R., Matsunaga, T., Ogawa, Y., Ishihara, Y., Morota, T., Hirata, N., et al. 2010. Possible Mantle Origin of Olivine Around Lunar Impact Basins Detected by SELENE. *Nature Geoscience* 3: 533–36.

Zeng, X., Liu, D., Chen, Y., Zhou, Q., Ren, X., Zhang, Z., Yan, W., et al. 2023. Landing Site of the Chang'e-6 Lunar Farside Sample Return Mission from the Apollo Basin. *Nature Astronomy* 7: 1188–97.

Zhang, B., Lin, Y., Moser, D. E., Hao, J., Shieh, S. R., and Bouvier, A. 2019. Imbrium Age for Zircons in Apollo 17 South Massif Impact Melt Breccia 73155. *Journal of Geophysical Research: Planets* 124: 3205–18.

Zhang, N., Ding, M., Zhu, M. H., Li, H., Li, H., and Yue, Z. 2022. Lunar Compositional Asymmetry Explained by Mantle Overturn Following the South Pole–Aitken Impact. *Nature Geoscience* 15: 37–41.

SUPPORTING INFORMATION

Additional supporting information may be found in the online version of this article.

Figure S1. Petrographic images of 72415,53 thin section 72415,53 in BSE (upper image) and X-ray mapping (lower image). Most of the sample is olivine (colored orange). Pale pink areas are anorthite. Scale bar is 1 mm. Grid on (A) is for location of EMPA point analyses.

Figure S2. TS 72415,53 BSE image with grid map. Scale bar is 2 mm.

Figure S3. BSE image of 72417,1, comprising 10 fragments. Scale bar is 1 mm.

Figure S4. Fragment B of 72417, (A) BSE image of whole fragment, scale bar is 500 μm. (B) BSE image of the area shown as a square in (A), (C) X-Ray map of the same area, showing anorthite (dark green), spinel (purple), and diopside (bright green) inside an olivine clast (brown). Scale bar for images B and C is 50 μm.

Figure S5. Fragment F of 72417,1 type C symplectite. (A) BSE image of whole fragment, scale bar is 500 μm. (B) BSE image of the area shown as a square in (A), (C) X-Ray map of the same area, showing anorthite (dark green), spinel (purple), and diopside (bright green) inside an olivine clast (brown). Scale bar for images B and C is 50 μm.

Figure S6. Fragment A of 72417,1 type C symplectite. (A) BSE image of whole fragment. Scale bar is 500 μm. (B) BSE image of the area shown as a square in (A), (C) X-Ray map of the same area, showing anorthite (dark green), spinel (purple), and diopside (bright green) inside an olivine clast (brown). Scale bar for images B and C is 10 μm.

Figure S7. CT images of 72417,9003, showing (A and B) 2-D slice images of a type A Cr-spinel symplectite (white). Scale bar = 1 mm. (C) 3-D rendered image of 72417,9003 with silicate phase rendered with no transparency. Scale bar = 100 μm. (D) 3-D rendered image of 72417,9003 with silicate phase rendered with high transparency revealing Cr-spinel type A structure (red). Scale bar = 100 μm. (E) 3-D rendered image of 72417,9003 with silicate phase cropped to reveal Cr-spinel type A structure (red). Scale bar = 100 μm.

Figure S8. TS 72415,53 BSE soi images (compressed file).

Table S1. TS 72415,53 BSE grid map reference table (see Figure S2 for gridded image of sample).